Materials Handbook: Second Target Station Project

Editor: Yong Joong Lee

Last Update: December 15, 2023

Contents

Part I

Materials

Chapter 1

Aluminium Alloy 6061-T6

1.1 Radiation Effects

The aluminium alloy 6061 in the T6 heat-treated condition is widely used in the high particle dose area surrounding the target. Aluminum 6061-T6 has a small scattering and absorption cross-sections to protons and neutrons, which leads to a minimum loss of protons and neutrons. It is the most favoured material for the proton beam window, which is under intense proton irradiation. Thanks to its better mechanical behaviour than those of solution annealed 5-series aluminium alloys under a high dose of thermal neutron fluence, it serves as baseline material for the vessels containing cryogenic hydrogen, water and beryllium of the moderator-reflector assembly system.

Upon hadron bombardments, the mechanical properties of the Al6061-T6 degrades mainly due to the following particle-matter interactions, helium production that causes material embrittlement, displacement damage initiated by primary knock-on atoms that causes materials hardening and reduced ductility, and silicon production that causes material embrittlement.

1.1.1 Helium production and material embrittlement

High energy protons and neutrons mainly via (p, α) and (n, α) reactions. Figure 1.1 shows the helium production cross-sections of proton and neutron in aluminum. With the increase of particle energy, the helium production cross section increases.

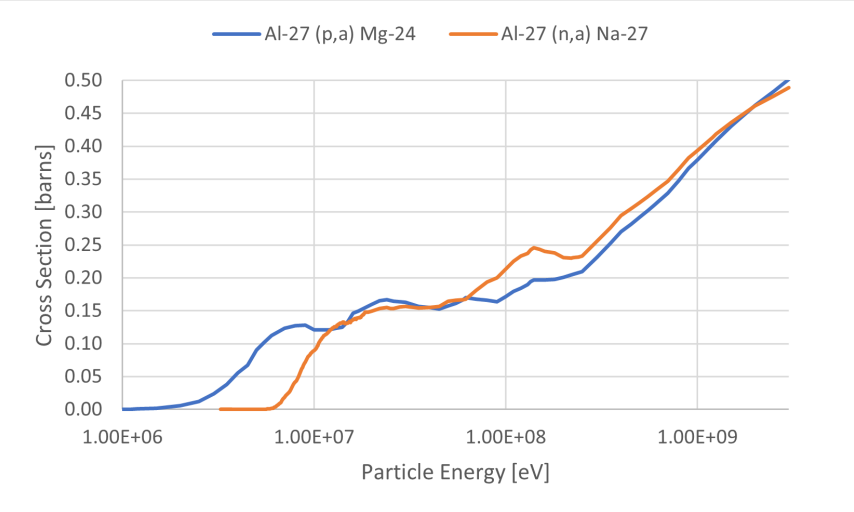

Figure 1.1: The helium production cross-sections of proton and neutron in aluminum.

Radiation induced helium in aluminum alloys cause helium embrittlement at a high helium concentra-

tion. There are scarcity of data of radiation induced helium embrittlement effects in Al6061-T6 available. Here, we take the data from the post irradiation examination of the beam window of the SINQ Target-9 at PSI as a guiding reference [1]. The beam window of the SINQ target-9 is made of Al5754-O $AlMg_3$, and it received the maximum fluence of $8.59{\cdot}10^{21}$ 570 MeV protons per square centimetres during 2011 and 2012. The high intensity proton beam and backscattered neutrons caused the calculated maximum displacement damage of 8.85 dpa, maximum helium production of 2447 appm, and maximum hydrogen production of 4853 appm. The tensile tests of the specimens taken from the BEW of the SINQ target-9 with the highest radiation damage showed a brittle behaviour with less than 2% of total elongation [2]. Figure 1.2 shows the tress-strain curves correlated with different displacement damages. The curve corresponding to 8.5-8.8 dpa corresponds to the peak helium concentration higher than 2300 appm. The tensile test results indicate strong irradiation hardening and embrittlement effects. The reduction of the uniform and total elongations of the $AlMg_3$ specimens at doses above 2.7 dpa is due to the high density helium bubbles at grain boundaries [3].

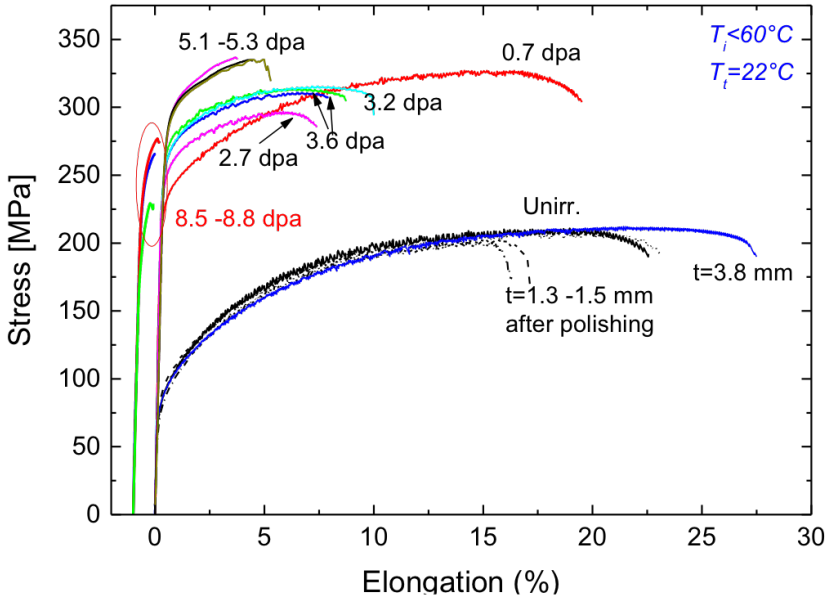

Figure 1.2: The stress-strain curves correlated with different radiation damages.

1.1.2 Displacement damage initiated by primary knock-on atoms

In spallation target environment, the SNS MARK-I moderators have received the highest displacement dose. The design lifetime of the SNS moderator is 30,000 MWh, which is set by the consumption of thick Gd poisson sheets [4]. The neutronics calculation for the SNS moderator system shows that the maximum radiation damage in the vessel is 7 dpa/SNS-year [4], where one SNS-year corresponds to 5000 operation hours of 1.4 MW beam. This indicates that the SNS moderator vessel should have received a maximum displacement damage of 30 dpa at the end of its project lifetime. This dpa number is higher than the one reached in the beam window of proton bombareded SINQ target at PSI shown in Fig. 1.2.

1.1.3 Silicon transmutation that causes material embrittlement.

The aluminum alloy 6061 in the T6 heat-treated condition is widely used as the material for the cold moderator containers at existing spallation sources, SNS, LANSCE and J-PARC. The properties of Al-6061-T6 are reviewed in detail in the AFCI handbook [5]. Irradiation in the fission neutron spectrum at 423 K and below can introduce significant hardening and embrittlement effects [6]. This is primarily due to the transmutation of aluminum to silicon induced by thermal neutron flux.

$$^{27}\mathrm{Al} + \mathrm{n_{th}} \rightarrow {}^{28}\mathrm{Al} + \gamma\,;\ {}^{28}\mathrm{Al} \rightarrow {}^{28}\mathrm{Si} + \beta^{-}. \tag{1.1}$$

However, the reduction of ductility saturates at high irradiation doses and the total elongation maintains at above 8% at a thermal neutron (the neutrons with energy less than 0.414 eV) dose of $3 \cdot 10^{23}$ neutrons/cm^2, as shown in Fig. 1.3. The thermal flux $3 \cdot 10^{23}$ neutrons/cm^2 corresponds to approximately 5 weight-% silicon content increase.

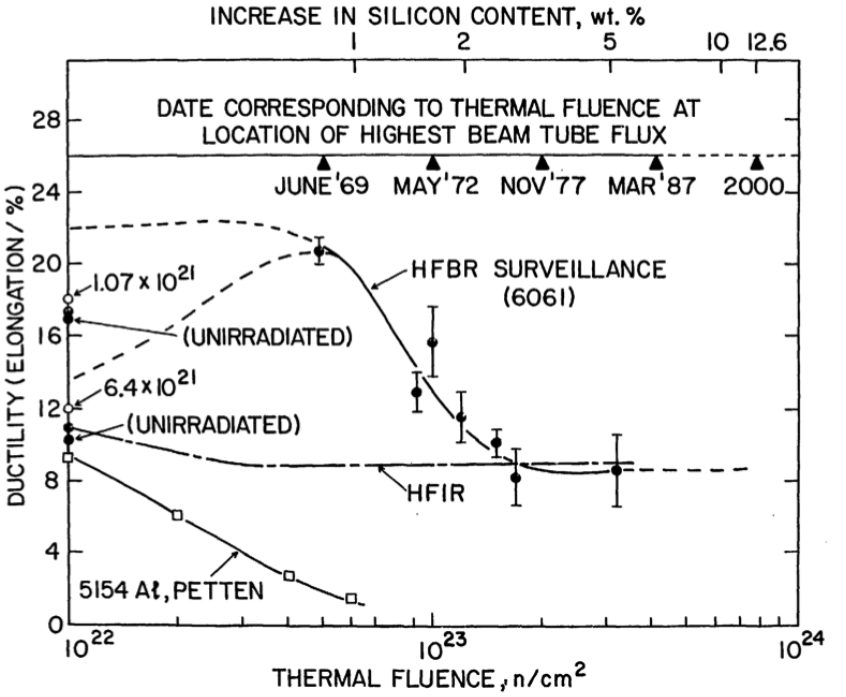

Figure 1.3: The effect of thermal neutron radiation on silicon content of 6061 Al [6].

The saturation of the degradation in total elongation also has been reported in Ref [7]. Aluminium 6061-T6 rods irradiated in the BR2 reactor at SCK-CEN in Belgium have been studied. These rods stem from a beryllium plug which has been removed in 2002 after 32 years irradiation in the beryllium matrix. The plug was cooled by light water, and the mean temperature of the rods is estimated to be 500 °C. The ratio of the thermal neutron flux ($E < 0,625$ eV) to the fast neutron flux ($E > 0,9$ MeV) is close to 6. Tensile tests were performed at different fluences, $1.3 \cdot 10^{23}$ n_{th}/cm^2 and $2.0 - -2.3 \cdot 10^{23}$ n_{th}/cm^2. The yield and tensile strength increased with the thermal fluence by a factor which is limited to 1.5 at $2.3 \cdot 10^{23}$ n_{th}/cm^2. The total elongation decreases from about 9% in the non-irradiated state to values between 4 and 5% at both tested fluences. The important result is that the total elongation tends toward a limit and that the alloy keeps a certain level of ductility at the highest fluences. This is confirmed by measurements of the necking parameter at fracture. The ductility reaches his minimum value at 75 °C.

1.2 Lifetime Crieria

1.2.1 Lifetime limited by Radiation Damage

The design basis maximum radiation induced helium concentration limit of Al6061-T6 is advised to be 2400 He-appm. This is based on the assumption that Al6061-T6 has similar helium embrittlement behavior as Al5754-O. As described in Sec. 1.1.1, the degradation of material property was attributed to increasing helium concentration. The beam window of the SINQ target made of Al5754-O has shown successful operations record with maximum radiation induced helium concentration of 2447 He-appm.

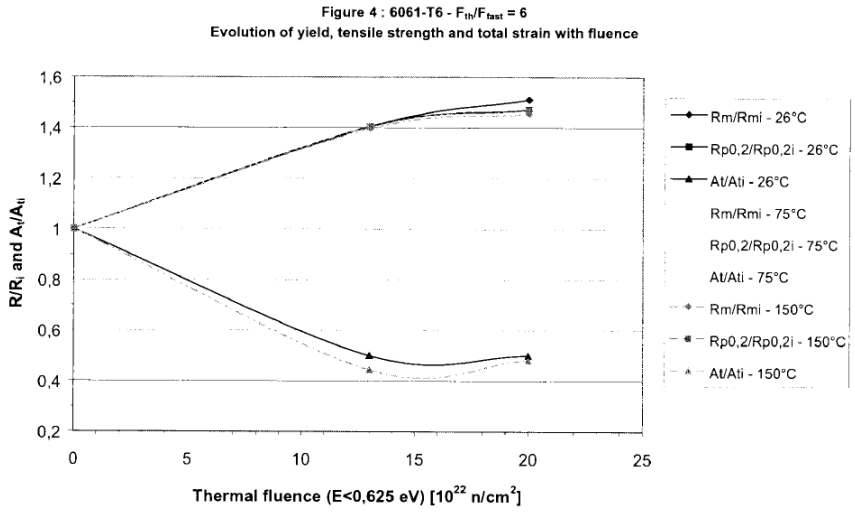

Figure 1.4: The effect of thermal neutron radiation on the mechanical properties of 6061 Al [7].

1.2.2 Lifetime limited by displacement damage initiated by primary knock-on atoms

The design basis maximum displacement damage limit of Al6061-T6 is advised to be 30 dpa. In the spallation environment, the moderator-reflector vessel of SNS has received a highest displacement damage, which is estimated to be 30 dpa; see Sec. 1.1.2. There has been no reported failure of the vessel.

1.2.3 Lifetime limited by thermal neutron fluence and silicon embrittlement

The design basis maximum thermal neutron fluence limit of Al6061-T6 is advised to be $1.8{\cdot}10^{22}$ $n_{thermal}{\cdot}cm^{-2}$. This follows the French nuclear code RCC-MRx [8] which defines the negligible radiation damage limit with the thermal neutron fluence of $1.8{\cdot}10^{22}$ $n_{thermal}{\cdot}cm^{-2}$ in Al6061-T6. This corresponds to about 0.3% of silicon yield in aluminium; see Sec. 1.1.3.

Chapter 2

Austenitic Steel 316L

2.1 SCOPE

This report summarizes material properties of solution annealed austenitic steel 316L with an aim to serve for the development and design activities to build SNS Second Target Station at ORNL.

2.2 APPLICATIONS AND TOP LEVEL REQUIREMENTS

2.2.1 Application of solution annealed austenitic steel 316L for STS

Solution annealed 316L is widely used as structural material in STS, particularly for water cooled components subject to particle irradiations.

2.2.2 Product Forms

2.2.3 Top Level Requirements

Cobalt Impurity

Guide on maximum allowed cobalt impurity in high radiation area at STS In high radiation area, the cobalt impurity in stainless steel components shall be kept below 0.2 weight-%. This is a decision taken, considering the cobalt impurity induced activation issues summarized below.

Cobalt impurity in stainless steel and radiation dose Though cobalt is not an alloying element, austenitic steel contains at least trace amounts of cobalt. Depending on the grade, the cobalt impurity in austenitic steel can reach up to 0.6% [9]. Naturally occurring cobalt is composed of one stable isotope, ^{59}Co. In thermal neutron rich environments, ^{60}Co is produced by neutron capture. The cross section for ^{59}Co(n, γ)^{60}Co is shown in Fig. 2.1. The ^{60}Co is a long living isotope with a half-life of 1925.28 days. It decays to ^{60}Ni by emitting high energy gammas with 1.17 MeV and 1.33 MeV. For these reasons, stainless steel having a high cobalt impurity in the target environment can become a main radiation source during in-beam operation, and post-irradiation handling, maintenance and storage. Therefore, the cobalt impurity in the components made of stainless steel in the target monolith is recommended to be based on ALARA (as low as reasonably achievable) principle. This section attempts to set the cobalt impurity limit in stainless steel components for the STS project, based on ALARA.

Cobalt impurity limit in stainless steel in reactor environment According to TBM which is technical regulations for Swedish NPPs, the cobalt content must not exceed 0,05 wt-% in the reactor vessel or its internal parts [11]. This requirement is also valid for areas larger than 10 m^2 outside the reactor vessel if the areas are exposed to water, which thereafter may enter the reactor vessel without passing through and ion exchanger. For areas smaller than 10 m^2 the cobalt content must not exceed 0,20 wt-% in components that are in contact with water that may enter the reactor unless the water first is passing through an ion exchanger. These requirements are based on the fact that corrosion product containing a

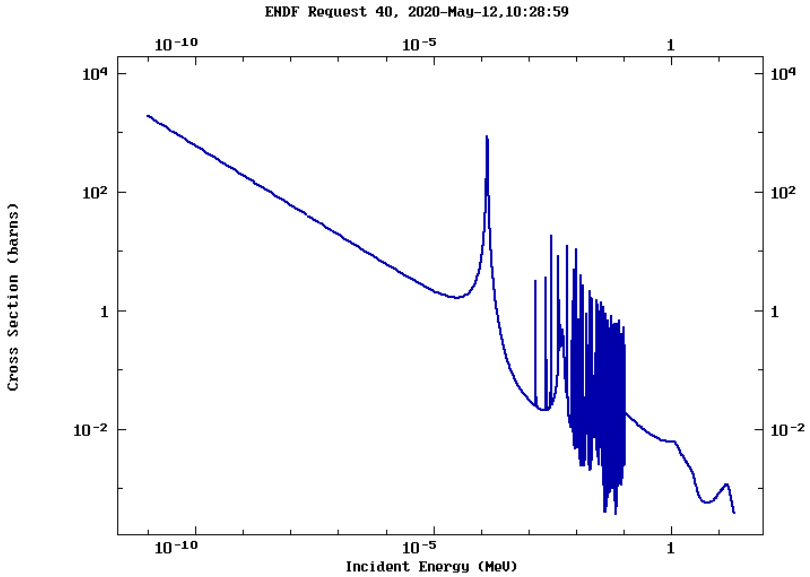

Figure 2.1: The ^{59}Co(n, γ)^{60}Co cross section [10].

high cobalt content are spread with the reactor water into the core where they are activated. Thereafter they are again distributed into the systems and are deposited in different components as extremely severe radiation sources.

Cobalt impurity limit from cooling water activation perspective In case the stainless steel is water cooled, there is a risk that the corrosion product containing a high cobalt content can activate the cooling water significantly. From the operational experience of the FTS, this risk of high cobalt impurity induced water activation is considered to be only marginal. The water sample data obtained on June 7, 2021 from the LW2 loop which cools the target shroud made of SS316L and PBW made of inconel showed the specific ^{60}Co activation 67 Bq·l^{-1} (1.8 pCi·ml^{-1}) as measured by gamma scan [12]. It is below the WHO guidance level for ^{60}Co in drinking-water, which is 100 Bq·l^{-1}. The cobalt impurity in SS316L used for the target shroud is 0.18 wt-%. Though this cobalt impurity level does not fulfill the requirement for the reactor vessel material, the water contacting surface area of the LW2 loop is much smaller than reactor vessel components. Furthermore, there is about three orders of magnitudes in radiation power between the reactor and the spallation source, which results in a correspondingly large difference in ^{60}Co production rate. These facts explains the low ^{60}Co activation in the LW2 loop despite the cobalt impurity in the target shroud is not of a nuclear grade.

Cobalt impurity limit from activation and shielding perspective Being irradiated by thermal neutrons in target environment, the stainless steel with a high cobalt impurity becomes a long-living gamma source, during in-beam operation, and post-irradiation handling, maintenance and storage. In this regard, it is important to specify cobalt impurity limit in procuring austenitic steel raw materials that are used for STS. However, requiring a low cobalt content to a nuclear grade limits the availability of raw material. This does not necessarily increase the project cost, but it could cause a significantly longer than planned procurement lead time affecting the project schedule negatively. Therefore, it is important to know the cobalt impurity level which is ALARA from procurement perspective as well. Once decided, ALARA cobalt impurity should be specified as an STS engineering and raw materials procurement requirement. The maximally allowed cobalt impurity will then serve as the cobalt content in stainless steel for the activation and shielding calculations, assuring conservatism in design.

2.3 RADIATION EFFECTS

2.3.1 Radiation Induced Stress Relaxation

Guide on Applying Radiation Induced Stress Relaxation Data for STS Target Systems Design

Based on the reviewed data on irradiation stress relaxation presented in the subsequent Sec. 2.3.1, we conservatively anticipate that about 60% of the preload in bolts and springs made of austenitic stainless steel will be relaxed (i.e., 40% of the preload will be retained) in STS target environment at 3 dpa. For reference, the maximum displacement damage of 3 dpa in stainless steel target vessel can be reached approximately in 5 years of full beam power proton beam operation. In this regard, we recommend taking 60% of preload loss due to radiation damage, in applying bolting and spring solutions for beam intercepting systems at STS.

Review of Existing Data on Irradiation Stress Relaxation

Radiation induced stress relaxation is an athermal process of plastic deformation of structural material under constant strain below the yield point in radiation environment, which depends on radiation damage and stress. It causes loss of preload for bolting and springs in target environment and its aging effect on the systems exposed to high proton and neutron radiations needs to be evaluated.

Empirical formula have been developed for estimating stress relaxation as a function of initial stress and neutron dose. In the following, data and empirical formula on neutron induced stress relaxation in stainless steel are summarized.

Figure 2.2 shows the irradiation stress relaxation of austenitic materials that are irradiated in the Halden thermal test reactor [13]. Note that fractional stress relaxation depends on fast neutron fluence,

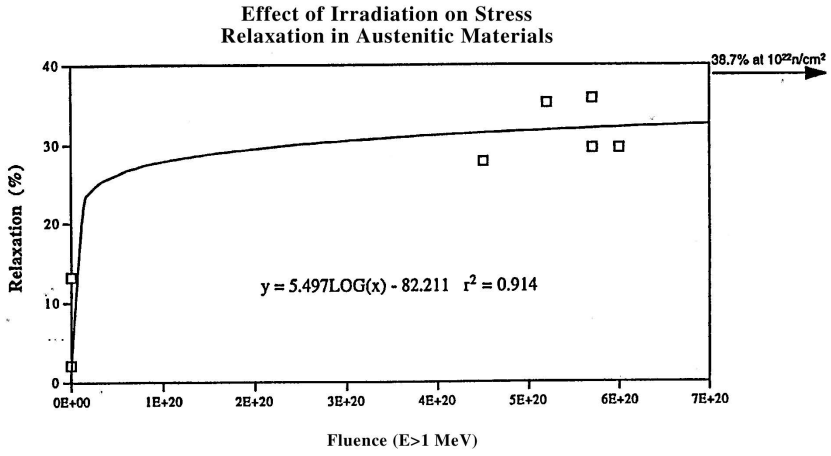

Figure 2.2: Irradiation stress relaxation of austenitic materials that are irradiated in the Halden thermal test reactor [13].

which is described by the following empirical formula

$$\left(1 - \frac{\sigma}{\sigma_0}\right)[\%] = 5.497 \log_{10} \phi_{E>1\,\mathrm{MeV}} - 82.211, \tag{2.1}$$

where σ is preload stress, σ is stress after irradiation, and $\phi_{E>1\,\mathrm{MeV}}$ is fast neutron fluence in $\mathrm{n}_{E>1\,\mathrm{MeV}}{\cdot}\mathrm{cm}^{-2}$. The fast neutron fluence in steel relates to displacement damage by multiplying it with (n, dpa) cross-section. At 1 MeV, the (n, dpa) cross-section for Fe is approximately given by 1000 barn=10^{-21} cm^2. In this regard, the graph in Fig. 2.2 shows stress relaxation up to 0.7 dpa radiation damage. Extrapolating Eq. (2.1) to 10 dpa, the fractional stress relaxation is estimated to be 38.7%.

Causey et al. evaluated irradiation stress relaxation with bent-beam specimens that were irradiated in thermal reactors [14]. Figure 2.3 shows the irradiation induced stress relaxation of solution annealed Type 304 stainless steel. At a fast neutron fluence of $8{\cdot}10^{24}$ $\mathrm{n}_{E>1\,\mathrm{MeV}}{\cdot}\mathrm{cm}^{-2}$ at 570 K, the fractional stress

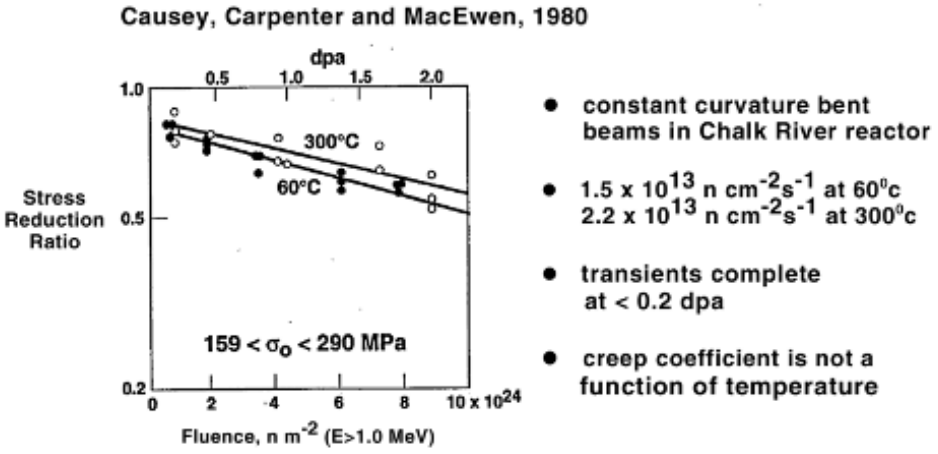

Figure 2.3: Irradiation stress relaxation of solution annealed Type 304 stainless steel [14].

relaxation is 35%.

Foster et al. presented the empirical formula for radiation induced stress relaxation of 20% cold worked Type 316 stainless steel [15], which is given by

$$\frac{\sigma}{\sigma_0} = \exp\left\{-E\left[A_1(1-\exp(-A_2 f)) + A_3 f\right]\right\}. \tag{2.2}$$

Here, $E = 1.93{\cdot}10^5$ MPa is elastic modulus of Type 316 stainless steel, f is the displacement damage in dpa. The empirically obtained coefficients A_1, A_2 and A_3 are given by $A_1 = 3.88 \cdot 10^{-6}$ MPa^{-1}, $A_2 = 4.3$ dpa^{-1} and $A_3 = 9.53 \cdot 10^{-7}$ MPa$^{-1}{\cdot}$dpa^{-1}. Figure 2.4 plots Eq. (2.2), where The upper and lower bound curves correspond to the 95% confidence intervals for the A1, and A3 coefficients. The bending stress relaxation

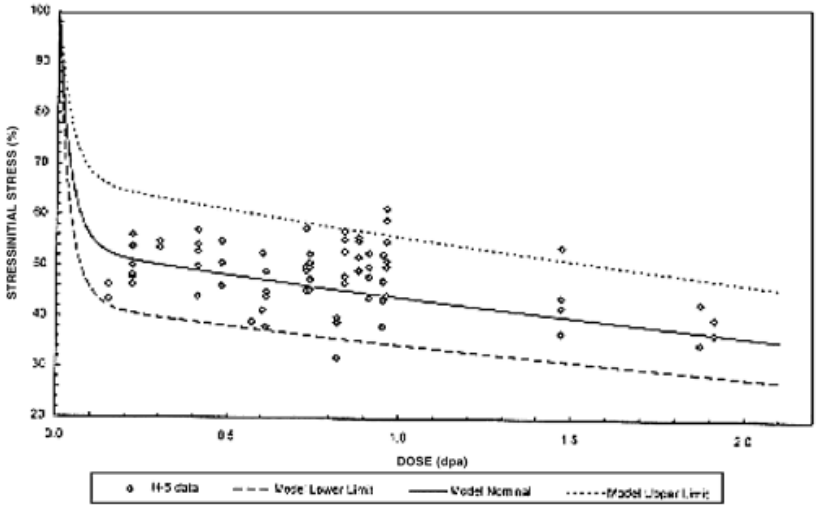

Figure 2.4: Irradiation stress relaxation of cold worked Type 316 stainless steel [15].

data points were obtained by irradiation in the EBR-II at different axial positions for two cycles at 370 °C.

Chopra and Rao reviewed existing data on irradiation stress relaxation [16]. Figure 2.5 shows irradiation induced stress relaxation data available at the time of publication. All the data points are bounded below by the trend line which is set by Alloy X-750 HTH bent beam at 57 °C. Note that stress relaxation data of austenitic steels are bounded above by 60% at 3 dpa.

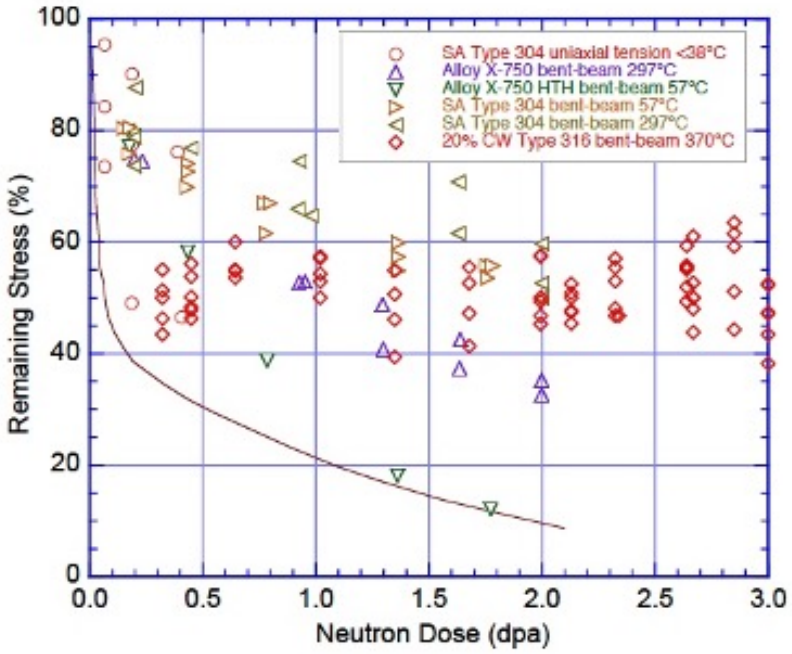

Figure 2.5: Irradiation stress relaxation data reviewed in Ref. [16].

Estimate of stress relaxation in 316L bolts at PBW

Figure 2.6 shows the location where bolting will be used to fix the inflatable seal to the proton beam window (PBW) frame. It is important to retain a good fraction of prestress in th bolts to keep the reuired seal function of the helicoflex at the location. Therefore, the extent of prestress loss in the bolts made of 316L has to be estimated.

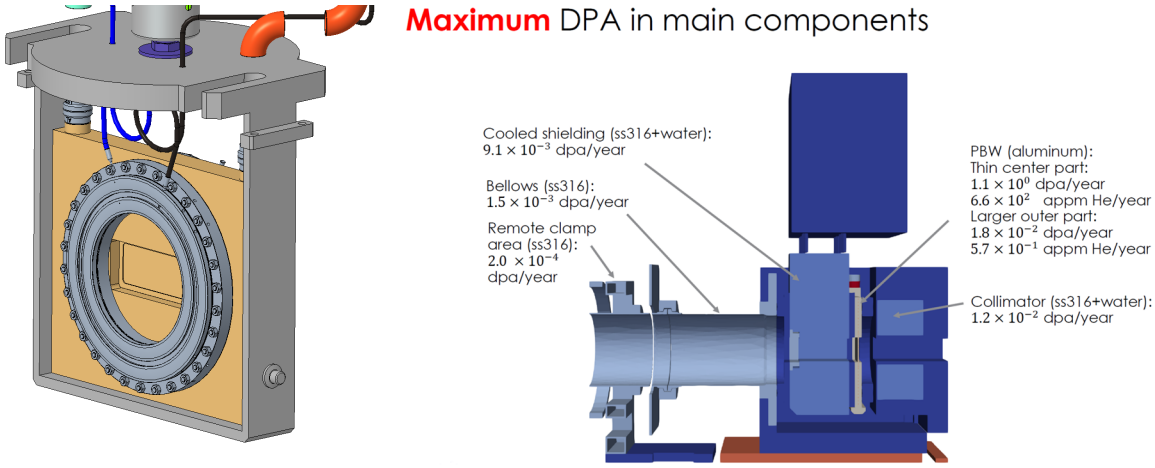

Figure 2.6: The locations of bolting that fix the inflatable seal to the proton beam window frame (left) and the calculated displace damage dose in the PBW and its supporting structure (right).

The calculated displace damage dose in the PBW and its supporting structure is also shown in Fig. 2.6. The damage dose in the stainless steel parts at the bolting location is less than the one in the collimator that is in the downstream region of the PBW. The collimator is exposed to a large flux of proton halos scattered by PBW and secondary neutrons. This indicates that the damage dose in the bolts will not exceed 0.1 dpa during the three years of PBW. For 0.1 dpa, the empirical formula (2.2) indicates

$$\frac{\sigma}{\sigma_0} = 0.76\,|_{0.1\mathrm{dpa}}\,. \tag{2.3}$$

This indicates that about a quater of prestress in the bolts is expected to be lost during the three year lifetime of the PBW.

2.3.2 Corrosion in radiation

The real-time corrosion rate of SS304L and SS316L are measured in a water system that was irradiated by 800 MeV proton beam at LANL [17]. The samples were adequately shielded from the irradiation cavity such that only the effects of water chemistry were investigated. Over the course of that irradiation period the corrosion rates for 304L SS, 316L-NG SS were less than 0.12 μm/yr. Figure 2.7 shows the measured corrosion rates of SS316L and SS304L. The irradiation period is divided into three separate categories in these plots: (1) pre-irradiation, beam off (indicated by negative days), (2) beam on 0.001-0.40 mA, corrosion insert only (days 0-10), and (3) beam on 1 mA, with all forward inserts in place in the beam upstream region (after day 10). From Fig. 2.7, it is difficult to clearly differentiate the corrsosion rates of

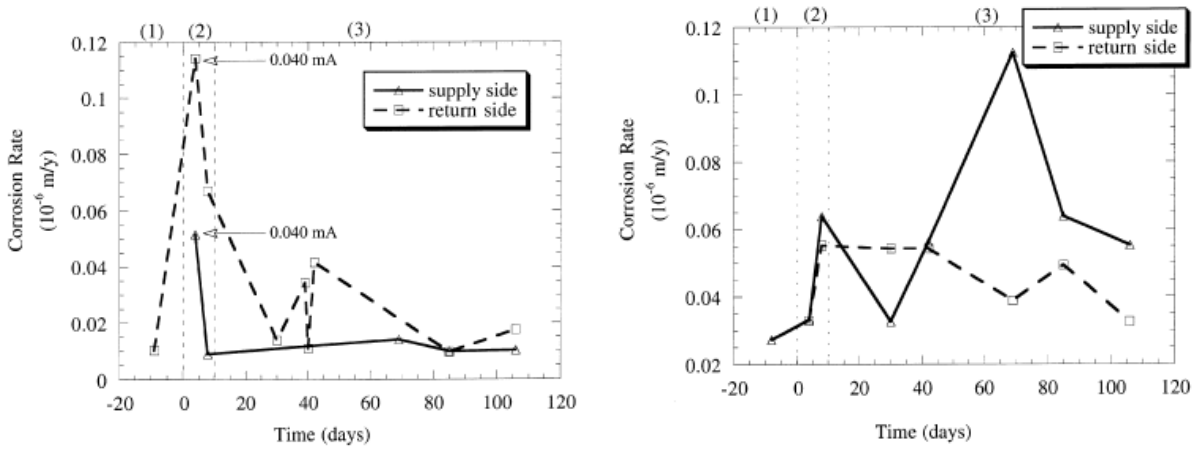

Figure 2.7: Measured corrosion rates of SS316L (left) and SS304L (right).

SS316L and SS304L, as the measured data seem to scatter randomly.

2.3.3 Irradiation Induced Stress Corrosion Cracking (IASCC)

Material selection and IASCC

The major spallation sources SNS and JSNS use SS316L for the water cooled structural components in spallation environments. It is due to a higher degree of corrosion resistance that SS316L provides when these are exposed to many types of chemical corrodents. In general, thanks to its additional molybdenum contents, the SS316L is known to be resistant to solutions of sulfuric acid, chlorides, bromides, iodides and fatty acids at high temperatures [18]. In this respect, particularly with concerns about the Irradiation Induced Stress Corrosion Cracking (IASCC) the SS316L served as the first choice material for engineering the water-cooled structural components in high hadron irradiation regions for STS.

Thermal sensitization

In welding the austenitic steel, thermal sensitization may occur in the heat affected zones of welds. Sensitization is caused by the formation of chromium carbides and a concomitant depletion of chromium in the grain boundaries, which increases the susceptibility to IASCC [19]. Figure 2.8 shows the combinations of time, temperature and carbon content that lead to sensitization of austenitic stainless steel. To mitigate the problem of thermal sensitization, low carbon grades of stainless steel such as type 316L are chosen for the IASCC susceptible parts of LWRs. These low carbon grade stainless steels have carbon contents of less than 0.03%. As indicated from Fig. 2.8, it is therefore difficult to form carbides on grain boundaries and thermal sensitization does not occur during the welding process.

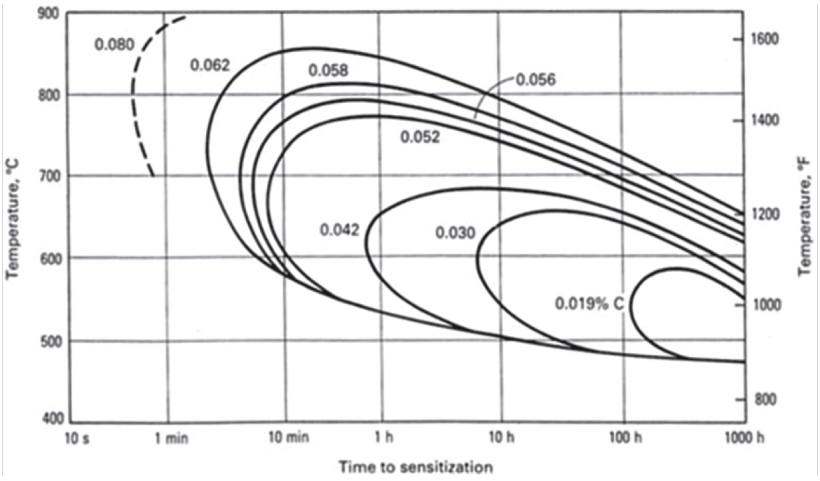

Figure 2.8: Time-temperature-transformation (TTT) diagram for austenitic stainless steel showing the combinations of time, temperature and carbon content that lead to sensitization.

Initiation threshold of IASCC

The threshold value of neutron fluence below which the materials can be considered not susceptible to IASCC in a PWR (Pressurized Water Reactor) environment is $2 \cdot 10^{21}$ n·cm^{-1} (3 dpa) [20]. For reference, the operating water temperature at PWR is typically around 300 °C. This fluence represents the dose at which the IASCC can be initiated at above the yield stress of the material. For the materials exposed to higher irradiation dose than this threshold value, a radiation damage dependent stress threshold has been compiled. Under the threshold stress for given radiation damage dose, the IASCC will not occur in a PWR environment. The compiled data on the correlation between the neutron dose and the threshold stress as percent of irradiated yield stress is shown in Fig. 2.9. The open symbols represent specimens that did not fail, and the closed symbols represent failed specimens. From Fig. 2.9 we note that none of the austenitic

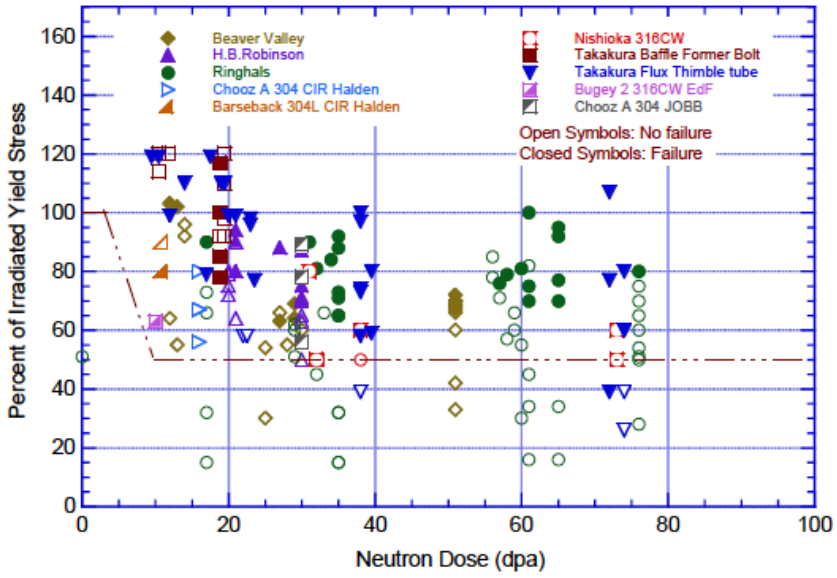

Figure 2.9: Stress as percent of irradiated yield stress vs. neutron dose for IASCC flaw initiation in austenitic stainless steels in a PWR environment [20].

stainless steel specimens failed below 40% of the irradiated yield stress level up to the neutron dose of 80

dpa.

Materials Reliability Program (MRP) proposed a screening curve for IASCC initiation of austenitic stainless steels as shown in Fig. 2.10. This curve is used to divide various PWR core internal components into different categories of aging management strategies during the initial screening process. This curve

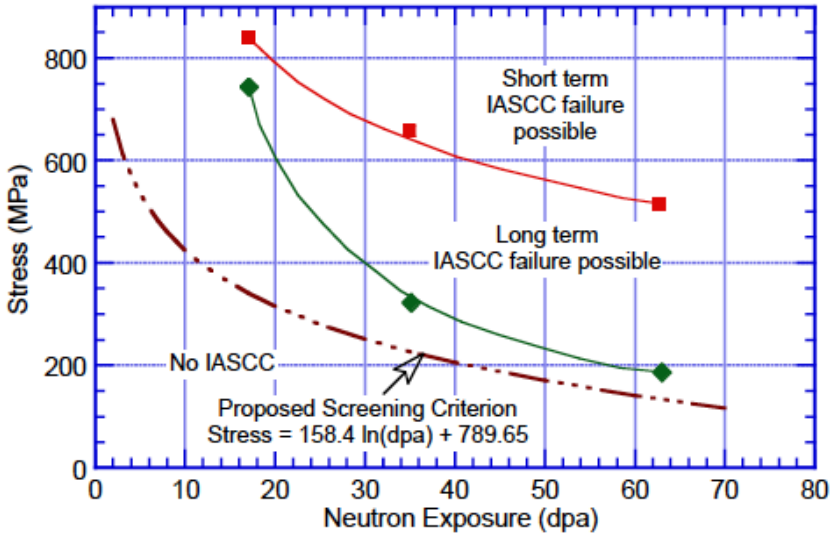

Figure 2.10: Time for initiation of IASCC in irradiated austenitic stainless steels as a function of stress.

proposes a conservative upper limit of the stress level in the 316L structural components in the STS spallation environments.

Compared to the reactor environments, the operational temperature of the 316L components in the STS target station is low, which should be below the boiling temperature of water at the design pressure of 4 bar. At temperatures lower than 300 °C, the radiation induced formation of the defects such as cavities and voids are suppressed in SS [20]. Therefore, the IASCC threshold criteria presented in Figs. 2.9 and 2.10 developed for the LWR reactor internal components aging guideline could be quite a conservative ones for the STS applications.

2.3.4 Irradiation Induced Hardening

SNS Target Window

Disk shaped samples were removed form the head region of the first and second targets at SNS [21]. The target vessel was made of SS316L, and microhardness tests were performed on the specimen with a damage dose of 4 to 5 dpa. The bulk hardness of the specimens increased with irradiation from, approximately 200 $HV_{0.05}$ Viker's microharness value before irradiation to 340 $HV_{0.05}$ after 4 to 5 dpa.

Baffle Bolt at CHOOZ

Hardness of a baffle bolts made of cold worked SS316, which were removed from the older French reactors CP0, was tested [22]. Figure 2.11 shows the hardness gradient along the bolts connected to irradiation level.

Complementary hardness tests on the baffle bolts made of cold worked SS316 have been done, which were removed from CHOOZ, a shutdown plant after 140,000 hours of operation [22]. Four bolts were used for metallurgical analysis with a cumulative dose between 0 and 22 dpa. The bolt of the core barrel, considered as unirradiated, shows a constant value of hardness along the bolt, equal to the unirradiated material value. The axial profile of hardness carried out on an irradiated bolt shows that there is a gradient of hardness between the most irradiated location (400 HV) and the least irradiated location (270 HV). The hardness of this bolt starts to decrease at 2.5 dpa and the maximum of hardening is reached for the most

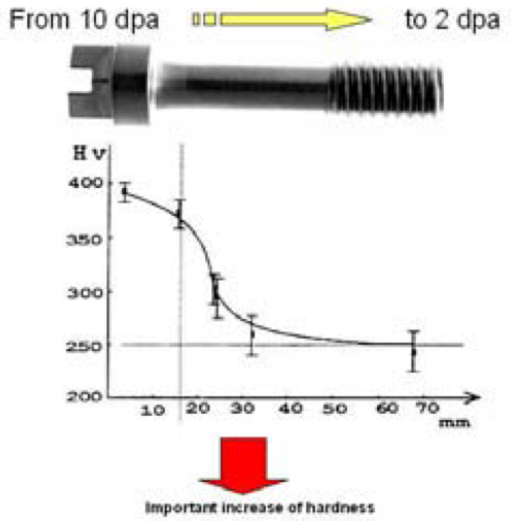

Figure 2.11: Hardness gradient along the bolt [22], which is correlated to dpa.

irradiated location (3.6 dpa). The hardness of the most irradiated bolt (between 10 and 22 dpa) indicates that hardness is homogeneous all along the bolt at 400 HV. It confirms the existence for these conditions of a threshold dose beyond which hardness does not vary anymore; this threshold is estimated between 3.6 and 10 dpa.

2.4 Lifetime Criteria

2.4.1 Lifetime Limited by Radiation Damage

Beam intercepting Devices

The design basis dose limit of proton beam intercepting structural devices made of 316L is advised to be 15 dpa. This proposal is based on existing data from post irradiation examinations (PIE) of 316L specimens that were proton irradiated in spallation environments. It is slightly higher than the administrative dose limit for the SNS target, which is currently 12 dpa for the inner layer of the water-cooled shroud [23].

The austenitic steels such as 316L(N) are one of the main classes of materials irradiated in the SINQ target irradiation program (STIP). Several kinds of austenitic steels from Europe, Japan and the USA have been irradiated to a maximum dose 17.3 dpa and a sample of the specimens have been tested [24, 25]. After irradiation at temperatures below 360 °C, the yield stress (YS) and the ultimate tensile strength (UTS) increased, while the uniform elongation or strain to necking (STN) and total elongation (TE) decreased with irradiation dose. The difference between YS and UTS of the specimens with radiation damage was much smaller than that of the control samples. This implies that the steels lose their work hardening capability after irradiation due to irradiation-induced hardening. For the dpa up to the tested maximum 17.3, the fracture surfaces showed a ductile fracture mode despite the reduced ductility. This indicates that the steels still have relatively good ductility at 10 to 20 dpa. The tensile data of the STIP specimens and the experience of SINQ targets indicate that SA 316L(N) can certainly withstand 10 dpa and more.

The PIE tensile tests of the SS 316L water-cooled beam window of SNS target samples show the vessel material increased in strength during operation but maintained an appreciable amount of ductility for dose values up to approximately 15 dpa [23].

Devices Subject to Radiation Damage by Secondaries

Stainless steel components in the neighborhood of the target that do not intercept the impinging proton beam are exposed to radiation damage induced by secondary neutrons. We categorize the components in three categories:

- Passive components without water cooling, which include the shielding blocks without water cooling.
- Components without water cooling but functionality is subject to radiation induced stress relaxation, which include the bolts and festeners.
- Components with water cooling, which include the core vessel beltline and inner core vessel shield blocks.

Dose limit of passive components without water cooling The design basis dose limit of the passive components without water cooling made of 316L is advised to not be set. These components are located in low dose area and water cooling is not required. For reference, the French nuclear engineering design code RCC-MRx defines the upper limit of negligible dose for the austenitic steel 316L with 2.75 dpa [8].

Dose limit of components without water cooling but functionality is subject to radiation induced stress relaxation The design basis dose limit of the components without water cooling but functionality is subject to radiation induced stress relaxation is advised to be 3 dpa beyond which no data on stress relaxation is available. In designing the initial residual stress for fastening, loss of 60% residual stress is advised to be accounted for, as existing data presented in Figs. 2.4 and 2.5 indicate.

Dose limit of components with water cooling The design basis dose limit of the components with water cooling is advised to be set based on the IASCC limit set in Figs. 2.9 and 2.10, where screening criterion is proposed by the following equation:

$$\sigma_{\max}\ [\text{MPa}] < 789.65\ [\text{MPa}] - 158.4 \ln(\text{dpa}). \tag{2.4}$$

For example, if the maximum stress of a component is 170 MPa, the lifetime is set to be 50 dpa.

Chapter 3

Beryllium

3.1 SCOPE

This report summarizes material properties of beryllium with an aim to serve for the development and design activities to build SNS Second Target Station at ORNL.

3.2 APPLICATIONS AND TOP LEVEL REQUIREMENTS

3.2.1 APPLICATION OF BERYLLIUM IN STS

Pure beryllium is used as reflector material for the Moderator Reflector Assembly (MRA).

3.2.2 Product Forms

Beryllium is commonly used for nuclear applications as a neutron multiplier and reflector material, where fission neutrons dominate. Different beryllium grades are summarized in Table 3.1, which are provided by the company MATERION [26]. Only the grades with nuclear applications are listed here. The commonly used production routes of nuclear grade beryllium for reflector applications are vacuum hot pressed (VHP) and hot isostatic pressed (HIP).

3.2.3 Top Level Requirements

Purity

The purity of the beryllium is of importance since certain impurities can, even at a low level, significantly impact the performance of the moderator due to the large absorption cross section of certain elements. The question is how pure the beryllium needs to be. The smaller the amount of impurities that activate strongly in the beam the easier it is to handle a beryllium reflector when it is exchange, possibly reuse the beryllium in the reflector for a new reflector or dispose of the beryllium.

In defining the requirements on beryllium purity for the STS reflector, the elemental specification used for the reflector filter at LANSCE serves as a good reference. The beryllium for the LANSCE reflector filter was purchased from Brush Wellman Inc. (now MATERION) in 2006. The amounts of each impurity in theLANSCE material were analyzed by Shiva Technologies, USA (Charge 5198). A material certificate includ-ing the elemental analysis data was obtained by Brush Wellman Inc. (Elmore, OH) in 2006 for LANSCE. Table 3.2 shows the analyzed elemental composition of beryllium used for the LANSCE reflector filter. The amounts of impurities are given as weight-ppm. This could be used as guiding elemental specification of beryllium for the STS reflector.

The neutron loss due to high impurity in the beryllium reflector-filter was measured in a beam line at LANSCE [27]. Table 3.3 shows the concentration of impurities measured in the beryllium used. The high impurity concentrations in Table 3.3 compares well with those for the high purity beryllium shown in Table 3.2. The excessive level of impurity in beryllium resulted in more than 15% of additional neutron

Grade	Production	Application	Description
S-200-F	VHP	Reflector and moderator of neutrons in nuclear environments, Materials test reactors	A versatile material selected when weight & inertia factors exceed those of lower cost aluminum.
S-200-F H	HIP	Reflector and moderator of neutrons in nuclear environments, Materials test reactors	A lightweight, high stiffness material, while maintaining typical metal properties. Selected when weight & inertia factors exceed those of lower cost aluminum.
S-200-F C	CIP	JET RF Antenna and Belt Limiter Tiles	Useful for Near Net Shapes (NNS) applications requiring lesser properties than obtained by HIP or VHP material. Tooling is reusable, good for parts required in the hundreds.
S-65	VHP	Nuclear Reflectors, Fusion energy applications: First wall in ITER and breeder pebbles	Where high purity is a consideration, or a high neutron flux is desired, it is very useful as both a moderator and reflector of neutrons.
S-65-H	HIP	Nuclear Reflectors, Tiles for JET and ITER like wall projects	Where high purity is a consideration, or a high neutron flux is desired, it is very useful as both a moderator and reflector of neutrons.

Table 3.1: Different beryllium grades that are provided by the company MATERION [26]. Only the grades with nuclear applications are listed here. The commonly used production routes for beryllium are Vacuum Hot Pressed (VHP), Hot Isostatic Pressed (HIP) and Cold Isostatic Pressed (CIP).

Element	Amount [wt-ppm]	Element	Amount [wt-ppm]	Element	Amount [wt-ppm]	Element	Amount [wt-ppm]
Be	>98.5	BeO	<1.5	Li	<0.01	Cd	<0.1
B	0.6	In	<0.05	C	<0.15	Sn	0.49
F	<0.5	Sb	0.27	Na	0.35	Te	<0.05
Mg	12	I	<0.01	Al	310	Cs	<0.01
Si	210	Ba	<0.005	P	2.2	La	<0.05
S	14	Ce	0.25	Cl	2.3	Pr	0.04
K	<0.05	Nd	0.21	Ca	7.1	Sm	<0.01
Sc	1.7	Eu	<0.01	Ti	130	Gd	<0.01
V	3.1	Tb	<0.01	Cr	90	Dy	<0.01
Mn	51	Ho	<0.01	Fe	940	Er	<0.01
Co	3.7	Tm	<0.01	Ni	190	Yb	<0.01
Cu	76	Lu	<0.01	Zn	0.22	Hf	1.5
Ga	0.08	Ta	<0.5	Ge	<0.5	W	10
As	<0.05	Re	<0.01	Se	<0.5	Os	<0.01
Br	<0.1	Ir	<0.01	Rb	<0.1	Pt	<0.05
Sr	0.74	Au	<0.5	Y	<0.5	Hg	<0.5
Zr	7.3	Tl	<0.01	Nb	0.57	Pb	0.1
Mo	7.8	Bi	<0.01	Ru	<0.01	Th	0.097
Rh	<0.1	U	3.6	Pd	<0.05	Ag	0.68

Table 3.2: Composition of the Beryllium used as reflector filter in the Lujan Target assembly. This composition is determined from an analysis of the S-65-F material from MATERION (former Brush-Wellman).

loss. For the reflector material for the STS, the effect of impurity on neutronic performance should be made, to determine requirements on maximum impurity concentrations in beryllium.

Element	Amount [wt-ppm]	Element	Amount [wt-ppm]	Element	Amount [wt-ppm]	Element	Amount [wt-ppm]
Cr	458	Cu	308	Mg	67	Fe	3250
Mn	75	Co	458	Ni	733	Zn	125
Ag	375	Cd	25	B	33		

Table 3.3: Composition of the beryllium with a high impurity concentrations initially used as reflector filter in the Lujan Target assembly.

The contents of elements that are highly activated in spallation and moderation environment shall be limited.The impurities that are to be constrained are, among others, B, Mg, Cs, In, Sb, Se, Sc, Cr, Co, Rh, Ag,Cd, Hf, Ta, W, Re, Os, Ir, Au, Hg, Th, Nd, Sm, Eu, Gd, Tb, Dy, Ho, Tm, Lu, and U. The level of the respective impurity in the beryllium should be determined by dedicated activation analyses and requirements for handling of irradiated beryllium at the end of service lifetime.

Grain Size

The effect of crystallite sizes on the performance of beryllium reflector at ESS was studied by Di Julio et al. [28]. The correlation between the crystallite size and neutron total cross section is shown in Fig. 3.1. The cold neutron brightness for the 42 beam ports at ESS is shown to degrade by about 2.5% with increasing crystallite size by 10 microns. EBSD of nuclear grade pure beryllium specimens typically show average grain sizes smaller than 10 microns. In this regard, it is reasonable to define smaller than 10 microns average grain size in beryllium as requirement for the STS reflector.

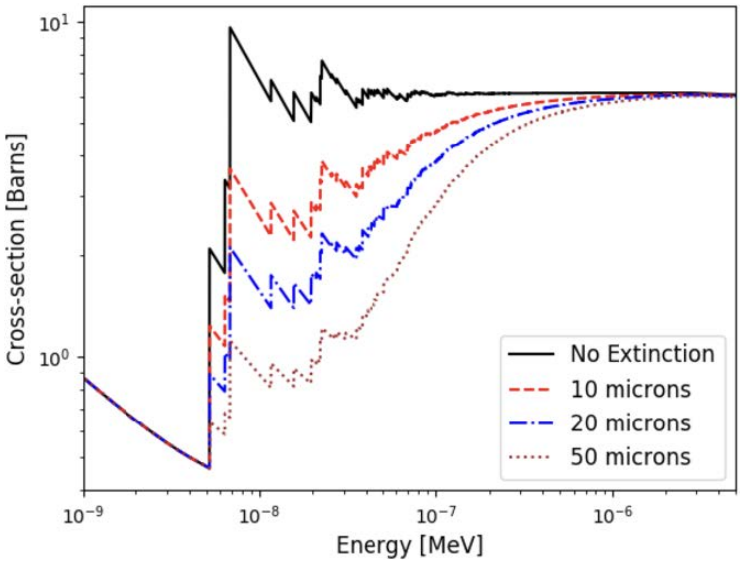

Figure 3.1: Neutron total cross-section for beryllium as a function of different crystallite sizes [28].

Miscellaneous Requirements and Lessons Learned from ESS

Other requirements and lessons to be considered in designing the STS reflector, which is learned from ESS experience during their beryllium vendor contacts, are summarized below:

- Requirements on disposal of used beryllium:

  - It is worth checking whether there is a way of recycling used beryllium.
  - The acceptable activation levels of radioactive beryllium has to be defined, in order that used parts can be refurbished into new beryllium reflector.
  - For now, most facilities store the irradiated Be.
- Vendor can provide materials certificate including elemental analysis upon request and additional fee.
  - It is worth asking vendor to provide us with old certificates of analysis from previous beryllium delivered to other customers, so we can see the actual amount of impurities in the Be.
- It is worth asking vendor to provide us with several beryllium sample pieces of different grades. These samples could be used for grain structure characterizations followed by neutron transmission measurements.
- It is worth asking vendor to provide us with information about:
  - their surface finish, e.g. chemically etched, machined, etc.,
  - the production process of beryllium of different grades of our interest.
- The recrystallization temperature of beryllium is above 800–1000 °C.
- No issues with directly cooling beryllium with water is not identified, though there is not enough information about beryllium erosion and corrosion in high radiation environment. It is important maintain high water purity.
- Silver and copper alloys can be used to surface bind beryllium to metal or aluminum.
- Hot isostatic pressed beryllium (S200FH) has little anisotropy compared to vacuum hot pressed S200F.
- A vendor suggested to have a “dome-shaped” piece of reflector than a ”cube-shaped.” It requires less material for less cost.
- A vendor suggests that the design with the water-lines running inside the beryllium would be easy enough to fabricate and save cost. As it can be manufactured from one piece.
- Internal radii shall be larger than 0.2 mm to avoid cracks.
- For the geometry of the ESS reflector, wire cutting is the most likely production method. Limitation could be its height (maximum 250 mm). The gaps must be larger than 2 mm, which is a drilling requirement.
- Beryllium can be welded with aluminum fillers.

3.3 Lifetime Criteria

3.3.1 LIFETIME DUE TO RADIATION INDUCED SWELLING

Neutron irradiation leads to complex changes in the micro-structure of beryllium, which may lead to swelling resulting from the formation of helium bubbles. There are two important pathways for gas production. One is the (n, 2n) reaction in which the ^{9}Be is reduced to ^{8}Be, which then splits into two ^{4}He atoms,

$$^{9}\mathrm{Be} + \mathrm{n}_{\mathrm{E>2.7MeV}} \rightarrow {}^{8}\mathrm{Be} + 2\mathrm{n}\,;\, {}^{8}\mathrm{Be} \rightarrow 2\,{}^{4}\mathrm{He}. \tag{3.1}$$

The second is the (n, α) reaction in which the ^{9}Be absorbs a neutron and then splits to form a ^{4}He and a ^{6}He. The ^{6}He rapidly decays to become ^{6}Li. The ^{6}Li then reacts with a thermal neutron to produce ^{4}He and ^{3}H,

$$\begin{aligned} {}^{9}\mathrm{Be} + \mathrm{n}_{\mathrm{E>1.4MeV}} \rightarrow {}^{6}\mathrm{He} + {}^{4}\mathrm{He} \quad &; \quad {}^{6}\mathrm{He} \rightarrow {}^{6}\mathrm{Li} \\ &; \quad {}^{6}\mathrm{Li} + \mathrm{n}_{\mathrm{th}} \rightarrow {}^{4}\mathrm{He} + {}^{3}\mathrm{H}. \end{aligned} \tag{3.2}$$

Therefore, a large amount of helium and tritium may be produced in the beryllium reflector. Fusion materials studies concluded that for an irradiation temperature below about 400 °C, swelling of beryllium containing 1,500 appm of helium is less than about 1% [29, 30]. The low temperature beryllium swelling as a function of helium content is shown in Fig. 3.2.

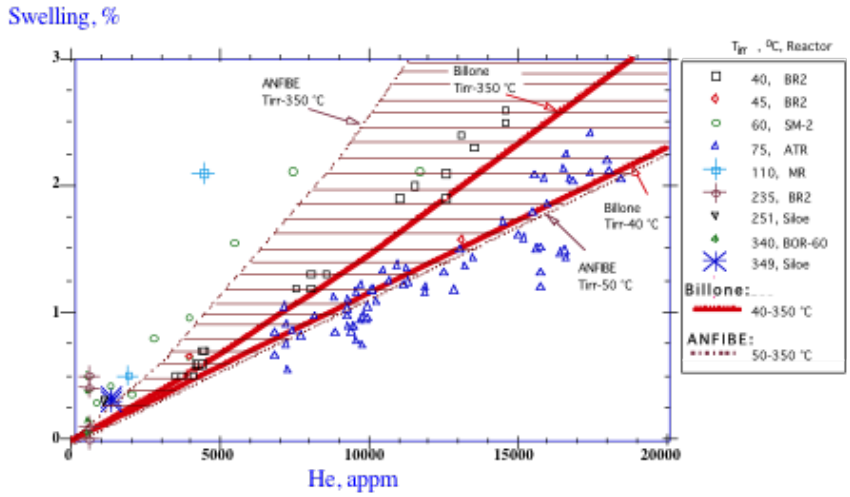

Figure 3.2: Low temperature beryllium swelling as a function of helium content [29, 30].

Helium bubbles produced in beryllium via (n, 2n) and (n, α) reactions may lead to swelling, which increases monotonically with irradiation dose. The swelling rate is correlated with helium production rate as shown in Fig. 3.2. At the time of writing this section, the helium production rate in beryllium reflector for STS is not calculated yet. However, the helium production rate can be conservatively estimated based on the calculation done for other high power spallation sources. The maximum helium production rate In the beryllium reflector at ESS is calculated to be 520 appm per 5 MW-year (25 GWh) integrated beam energy on target [31]. The helium production rate in beryllium reflector of the FTS of SNS has also been calculated by Franz Gallmeier [32]. The calculation shows that the helium production rate is 111 appm per 2 MW-year (10 GWh) integrated beam energy on target. Extrapolating these two numbers for helium production rates, the helium production in the beryllium reflector of STS is estimated not to exceed 1000 appm during its service lifetime. From Fig. 3.2 one reads that total helium production of 1000 appm in beryllium would cause about 0.1% volumetric swelling if the beryllium is kept at a temperature below 350 °C. This suggests that the structural failure of the beryllium container due to beryllium swelling would not happen during the lifetime of the MRA system at STS, where the lifetime is limited by ductility loss and radiation damage in the aluminum alloy canisters. Neutron irradiation at low temperatures will induce embrittlement as well. However, as the stress level in the reflector should not be high, the embrittlement may not cause a serious failure in the integrity of the beryllium volume during the lifetime of the MRA system.

3.3.2 LIFETIME DUE TO RADIATION INDUCED LOSS OF THERMAL CONDUCTIVITY

The radiation induced attenuated thermal conductivity of beryllium would increase steady state temperature gradient and maximum temperature in its volume. With the design of the reflector volume, the effects of decreased thermal conductivity on thermo-mechanical stress and temperature at water contact interface have to be analyzed, so that the reflector could be cooled sufficiently during the lifetime of the MRA system.

Thermal Conductivity

Unirradiated The thermal conductivity of beryllium depends on their density, purity, production method and processing, as compiled in Ref. [33]. Table 3.4 lists the temperature dependent thermal conductivities of beryllium with different production routes.

Temperature	**Thermal Conductivity [W·m^{-1}·K^{-1}]**			
[K]	Well-annealed polycrystalline Be of high purity	Hot-pressed Be after exposure of 1000 hrs at 1300 K	Hot-pressed Be	Cold-pressed Be
300	200	156	182	97
400	161	146	170	91
500	139	132	156	84
600	126	119	145	78
700	115	110	134	74
800	106	100	120	68
900	98.2	86	109	64
1000	90.8	80	96	61
1100	84.2	78	86	57
1200	78.7	75	84	55
1300	73.8	73	82	51
1400	69.4	-	-	-
1500	-	67	76	46

Table 3.4: The temperature dependent thermal conductivities of beryllium with different production routes [33].

The data points for the hot-pressed Be after exposure of 1000 hrs at 1300 K listed in Table 3.4 can be expressed in an analytic fitting as given below.

$$\lambda = 202.5 - 1.723 \cdot 10^{-1}\, T + 5.467 \cdot 10^{-5}\, T^2, \tag{3.3}$$

where the thermal conductivity λ is in [W·m^{-1}·K^{-1}] and the temperature T is in [K].

Irradiated: Thermal conductivity versus fast neutron fluence Neutron irradiation leads to complex changes in the micro-structure of beryllium, which may lead to a decrease in thermal conductivity. The relation between the fast (E > 0.1 MeV) neutron fluence and the decrease in thermal conductivity of beryllium is studied in Ref. [34].

Figure 3.3 shows the thermal conductivity of hot extruded (HE) beryllium before and after irradiation at 473 K up to a neutron fluence of $1.2{\cdot}10^{22}$n·cm^{-2}. Note that the thermal conductivity values are not isotropic. Note that the temperature dependence of the thermal conductivity gets less significant after irradiation.

Figure 3.4 shows the dependence of thermal conductivity of hot extruded (HE) beryllium irradiated at 343 K and 473 K on neutron fluence. For neutron fluences larger than $0.5{\cdot}10^{22}$n·cm^{-2}, the directional dependence of the thermal conductivity gets less significant.

For fast neutron fluences larger than $1.0{\cdot}10^{23}$n·cm^{-2}, the irradiated hot extruded and hot isostatic pressed beryllium samples show roughly about 20% of the thermal conductivity of unirradiated samples at 343 K and 40% at 473K. Figure 3.5 shows the comparison of thermal conductivity of different beryllium grades.

It is estimated that the maximum fluence in the beryllium reflector will be about $1.0{\cdot}10^{22}$n·cm^{-2} [32] during the lifetime of the moderator reflector assembly (MRA). In this respect, a conservative assumption of the thermal conductivity of beryllium at the end of MRA lifetime would be 50% of the unirradiated value. We recommend reflector design engineers to use the beryllium thermal conductivity, which is 50% of the unirradiated value presented in Table 3.4, in assessing the impact of irradiation on temperature and thermal stress.

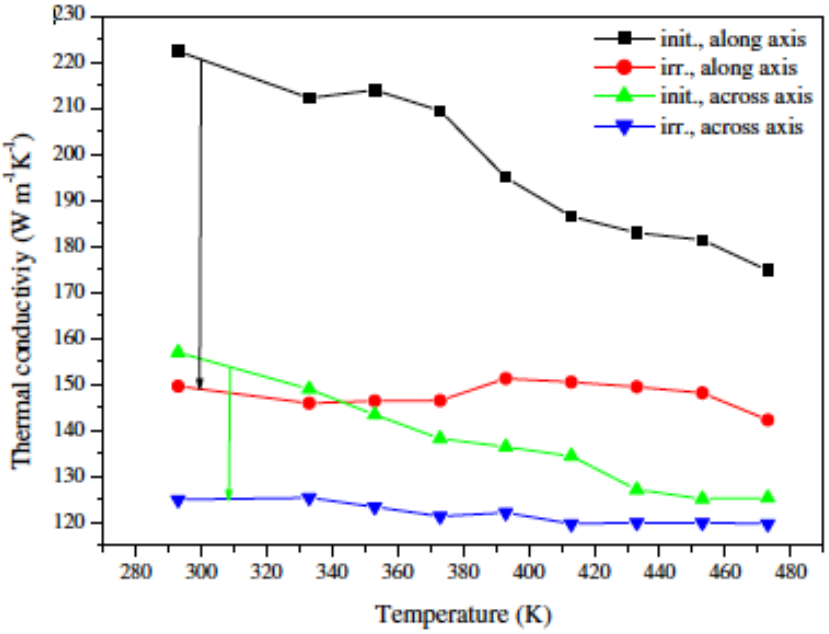

Figure 3.3: The thermal conductivity of hot extruded (HE) beryllium before and after irradiation at 473 K up to a neutron fluence of $1.2{\cdot}10^{22}$n·cm^{-2}.

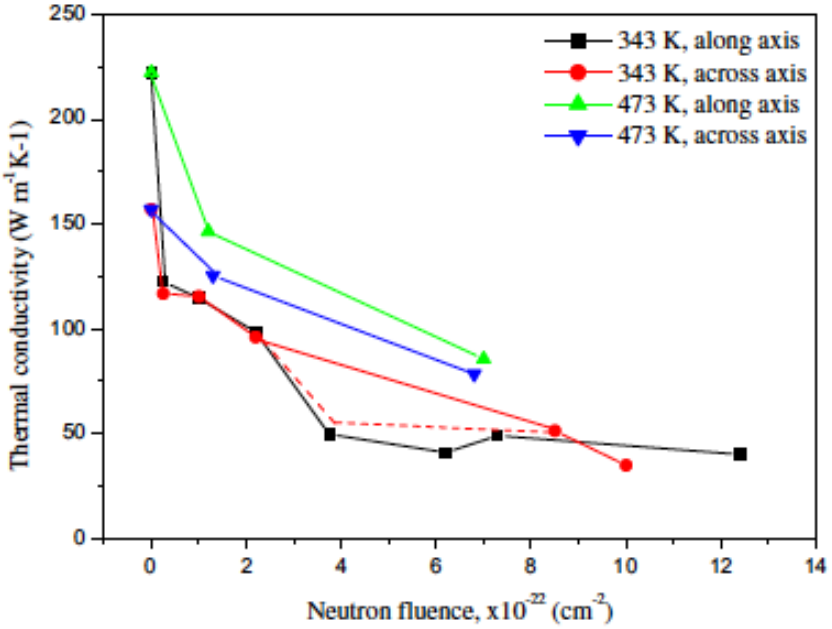

Figure 3.4: The dependence of thermal conductivity of hot extruded (HE) beryllium irradiated at 343 K and 473 K on neutron fluence.

Thermal conductivity versus radiation induced swelling Figure 3.6 shows the correlation between radiation induced swelling and thermal condutivity, which is compiled in ITER Materials Handbook [35].

The thermal conductivity can be conservatively expressed in an analytic equation given in Ref. [36].

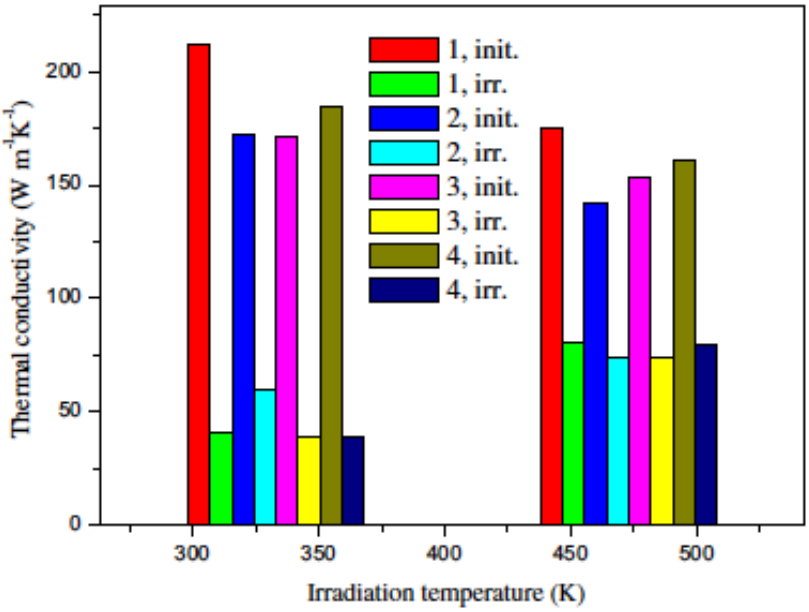

Figure 3.5: The comparison of thermal conductivity of different beryllium grades at irradiation temperatures 343 K (left) and 473 K (right). The garde 1 and 2 berylliums are hot extruded samples, and grade 3 and 4 berylliums are hot isostatic pressed samples. The fast neutron fluences are Φ_1 =1.24·10^{23}n·cm^{-2}, Φ_2 =0.77·10^{23}n·cm^{-2}, Φ_3 =1.20·10^{23}n·cm^{-2} and Φ_4 =1.20·10^{23}n·cm^{-2} at 343 K, and Φ_1 =0.70·10^{23}n·cm^{-2}, Φ_2 =0.98·10^{23}n·cm^{-2}, Φ_3 =1.27·10^{23}n·cm^{-2} and Φ_4 =0.53·10^{23}n·cm^{-2} at 473 K.

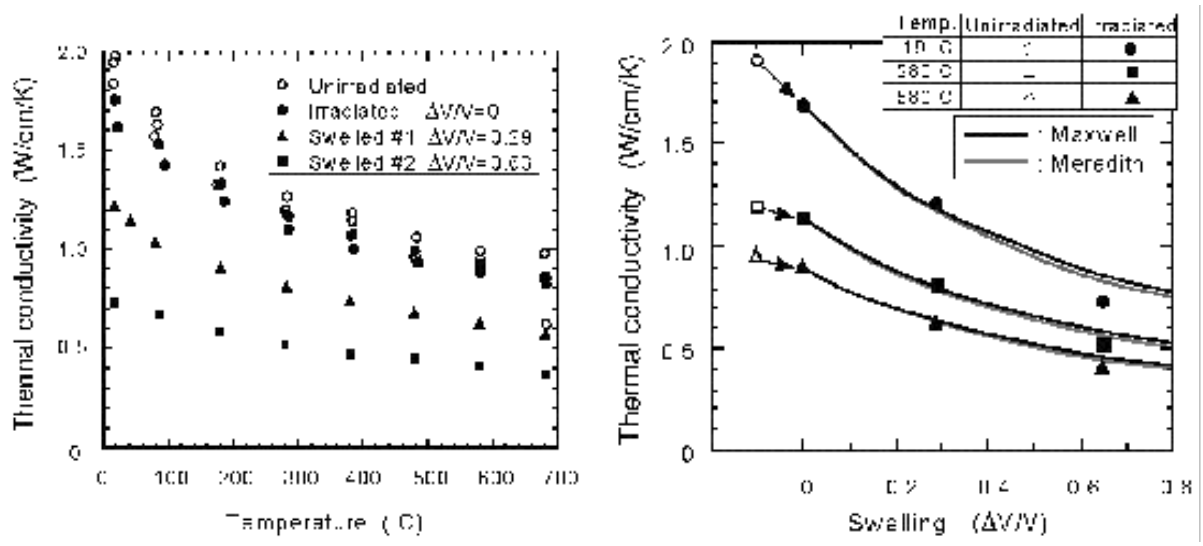

Figure 3.6: The correlation between radiation induced swelling and thermal condutivity, which is compiled in ITER Materials Handbook [35]. The unit of the swelling $\Delta V/V$ is given in percent (%).

Effect of swelling on the thermal conductivity is given by

$$\begin{aligned} \lambda_{\text{irrad}} &= \lambda_{\text{unirr}} \cdot f(\phi) \cdot S(\nu) \\ &= \lambda_{\text{n}} \cdot S(\nu), \end{aligned} \tag{3.4}$$

where λ_{irrad} is the thermal conductivity of neutron irradiated beryllium including swelling effect, λ_{unirr}

is the thermal conductivity of unirradiated beryllium, $f(\phi)$ is the contribution of defects generated by neutron irradiation and/or helium production, $S(\nu)$ is the contribution of swelling, ν is the volume ratio of produced helium voids, λ_n is the thermal conductivity of neutron irradiated beryllium except the swelling effect. The swelling effect function $S(\nu)$ is given by

$$S(\nu) = 8\frac{(2-\nu)(1-\nu)}{(4+\nu)(4-\nu)}. \tag{3.5}$$

The analytic fit provided by Eqs. (3.4) and (3.5) is compared in Fig. 3.6 with the measured data.

Once the swelling is estimated, the equation of Meredith given by Eqs. (3.4) and (3.5) can be used to predict the thermal conductivity of neutron irradiated beryllium at high temperature.

Chapter 4

Copper

Pure copper is a candidate thermal interface material for the target. With the progress of radiation damage, the density, thermal conductivity and mechanical characteristics change, and it is important to compile the existing knowledge about radiation damage behavior of copper to assess the structural robustness and lifetime of the target using copper. In this report, material properties of copper with a hadron radiation damages are summarized.

4.1 Radiation Effects

4.1.1 Irradiation Induced Degradation of Thermal Conductivity

The electrical resistivity and tensile properties of copper has been measured before and after fission neutron irradiation to damage levels of 0.5 to 5 dpa at temperatures between 100 °C and 400 °C [37]. Some of the specimens were irradiated inside a I.5 mm Cd shroud in order to reduce the thermal neutron flux. The electrical resistivity data could be separated into two components. a solid transmutation component $\Delta\rho_{\rm tr}$, which was proportional to thermal neutron fluence and a radiation defect component $\Delta\rho_{\rm rd}$, which was independent of displacement dose. The saturation value for $\Delta\rho_{\rm rd}$ was 1.2 nΩ·m for pure copper irradiated at 100 °C in positions with a fast-to-thermal neutron flux ratio of 5. Considerable radiation hardening was observed in all specimens at irradiation temperatures below 200 °C.

Figure 4.1 shows measured changes in electrical resistivity versus thermal neutron fluence for pure copper.The empirical law derived from the measurements is given by

$$\Delta\rho_{\rm total} = \Delta\rho_{\rm rd} + \Delta\rho_{\rm tr} = \Delta\rho_{\rm rd} + K\cdot\Phi_{\rm thermal}, \tag{4.1}$$

$$\Delta\rho_{\rm rd} = 1.2\,[{\rm n}\Omega\cdot{\rm m}], \quad K = 3.5\cdot10^{-25}\,[{\rm n}\Omega\cdot{\rm m}^3\cdot{\rm n}_{\rm thermal}], \tag{4.2}$$

where $\Phi_{\rm thermal}$ is thermal neutron fluence in $[{\rm n}_{\rm thermal}\cdot{\rm m}^{-2}]$. Note that the increase in the resistivity $\Delta\rho_{\rm rd}$ due to displacement damage saturates at above 0.1 dpa.

There is a linear correlation between the electrical conductivity and thermal conductivity following Wiedemann-Franz Law,

$$\kappa_{\rm Cu} = L_{\rm Cu}T\sigma_{\rm Cu}, \tag{4.3}$$

where $\kappa_{\rm Cu}$ is thermal conductivity, $L_{\rm Cu}$ is Lorenz number, and $\sigma_{\rm Cu}$ is the electrical conductivity of copper. The Lorenz number for copper is given by $2.23{\cdot}10^{-8}$ [W·Ω·K^{-2}] at 273 K and $2.33{\cdot}10^{-8}$ [W·Ω·K^{-2}] at 373 K. The radiation induced fractional reduction in thermal conductivity of copper is then given by

$$\frac{\Delta\kappa_{\rm Cu}}{\kappa_{\rm Cu:0}} = -\frac{\Delta\rho_{\rm total}}{\rho_{\rm Cu:0}+\Delta\rho_{\rm total}}, \tag{4.4}$$

where the subscript "0" denotes "unirradiated." For reference, the electrical resistivity of unirradiated pure copper is $\rho_{\rm Cu:0}$ =17.7 nΩ·m. For reference, the maximum annual neutron fluence in the copper volume of the Lasagna target is about 10^{23} ${\rm n}_{\rm thermal}\cdot$ m^{-2}·year^{-1} [38]. Plugging this number to Eqs. (4.1) and (4.2), equation 4.2 becomes

$$\frac{\Delta\kappa_{\rm Cu}}{\kappa_{\rm Cu:0}} = -\frac{1.2+0.035\,Y}{18.9+0.035\,Y}\,, \tag{4.5}$$

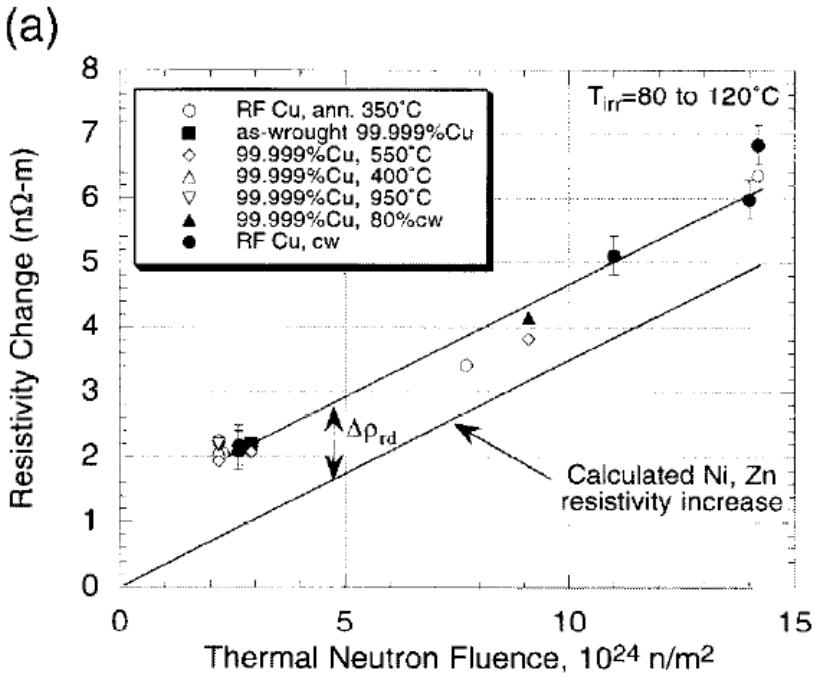

Figure 4.1: Measured change in electrical resistivity versus thermal neutron fluence [37].

where Y is number of beam-on-target years. For instance, after 10 years of target operation, the thermal conductivity of copper could be reduced up to 8%. After a few months of target operation when the maximum damage dose reaches 0.1 dpa, the displacement damage induced decrease in thermal conductivity manifests. The thermal conductivity is estimated to decrease by 6% within the first few months of target operation.

4.1.2 Irradiation Induced Void Swelling

Radiation induced void swelling becomes a concern at above ≃0.3 homologous temperature (the ratio of the absolute temperature of a metal to its melting point) where vacancies become mobile [39]. Void formation does not occur during irradiation of copper unless suitable impurity atoms such as oxygen or helium are present [40].

Residual impurity oxygen can have a significant effect on void swelling in copper. A number of neutron, ion, and electron irradiation studies have shown that voids are not formed in high-purity, low-oxygen copper over the wide range of irradiation temperatures. The oxygen content should be maintained below 10 wppm to minimize void swelling in copper [41]. For reference, thermodynamic-based calculations which predict that oxygen concentrations of 50 appm are needed to stabilize void formation in pure copper at 400 °C if other gases are not present [42].

The effect of helium production on void formation and swelling in copper is a significant concern for its spallation target applications. Significant enhancement of void formation and swelling was observed in copper under ion irradiation with simultaneous helium implantation. The void swelling increases with increasing particle fluence. A steady-state swelling rate of about 0.5%/dpa is observed in copper at high doses, and the swelling level can be as high as 60%. Low oxygen coppers irradiated by fast neutrons showed 2.6-4.8% swelling at 16.9 dpa (irradiation temperature 375 °C) and 14.0-15.1% swelling at 47.3 dpa (irradiation temperature 430 °C) [42]. It was pointed out that the important contribution of even small amounts of helium generation (via fast neutron transmutation effects) in enhancing the stability of void nuclei. The calculated minimum concentration of helium needed to stabilize the cavities nucleated in neutron-irradiated copper is a strong function of temperature, ranging from about 0.1 appm He at 200 °C to about 0.001 appm He at 400 °C. In fast reactor, helium generation rate in copper is about 0.1 appm/dpa.

Neutron irradiation of copper containing 18 wppm ^{10}B to 1.2 dpa for the irradiation temperatures of 182–500 °C. In fission reactor environments, ^{10}B captures thermal neutron and undergoes an instantaneous

βdecay to produce a high-energy αparticle and a high-energy ^{7}Li nucleus:

$$^{10}\mathrm{B} + \mathrm{n}_{E<20MeV} \rightarrow ^{11}\mathrm{B} \rightarrow \alpha + ^{7}\mathrm{Li}. \tag{4.6}$$

Therefore, the irradiated ^{10}B containing copper in a fission reactor will have about 100 appm helium at the end of the irradiation time. Figure 4.2 showes that the peak swelling temperature and the lower swelling temperature limit shifted to lower values.

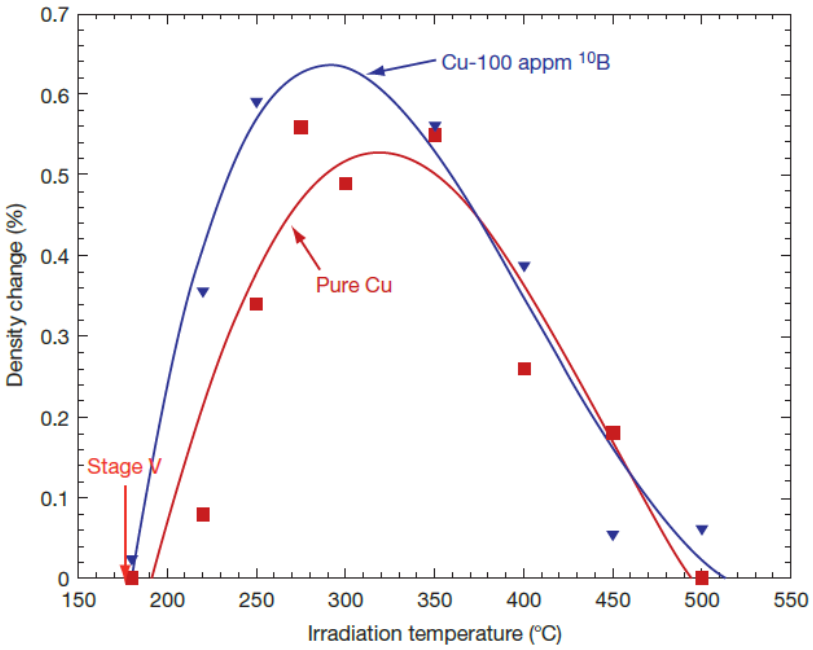

Figure 4.2: Swelling in pure copper and Cu–B alloy. [41].

There are other radiation parameters than dpa and helium production that affect the void swelling in copper. An order of magnitude decrease in neutron flux which is correlated to lower dpa rate can lower the peak swelling temperature by about 20 °C. The peak swelling temperature shift can be as high as 165 °C between neutron irradiation (10^{-7}·dpa·s^{-1}) and ion irradiation (10^{-3}·dpa·s^{-1}). For reference, the dpa rate in copper in the STS target is about $5{\cdot}10^{-8}$·dpa·s^{-1}, which is in the order of 10^{-7}·dpa·s^{-1}.

As a design basis void swelling rate, we use the plot of "Cu-100 appm ^{10}B" in Fig. 4.2 as a reference relation between the swelling and temperature for a helium fraction of 100 appm in copper. The graph will be scaled to the dpa and helium production rates in the copper thermal interfacing volume of the present target design. The dpa and helium production rates depend on the size of beam footprint on the target. For a beam footprint size between 60 and 90 cm^2, preliminary particle transport calculations sgow that the maximum dpa rate in the copper volume is about 1 dpa/year and the helium production rate is about 50 appm/year. The helium production rate in copper is far more aggressive in the STS target compred to those irradiated by fission, fast and fusion neutrons. As helium contributes significantly to void swelling, it is fair to take extra conservatism. Until more data on radiation induced void swelling in copper in spallation environments are known, we propose to use the "Cu-100 appm ^{10}B" curve with the following modifications:

- The peak of the "Cu-100 appm ^{10}B" curve is scaled to have the peak at 0.5% for the displacement damage of 1 dpa. The peak is scaled linearly with dpa numbers.
- The "Cu-100 appm ^{10}B" curve is shifted along the temperature axis so that it has void sweliing onset point at 160 ∘C.

4.1.3 Irradiation Induced Helium Embrittlement

Two batches of pure copper tensile specimens were tested, which were respectively irradiated by 40 MeV helium beam using cyclotron and by fast neutrons in the BOR-60 reactor [43]. The helium beam irradiation

deposited up to 40 appm helium in the specimens with negligible dpa. The helium irradiation temperature in the specimens were about 100 °C. The specimens in the BOR-60 received fast neutron fluence up to 7.7–7.9·10^{21} n·cm^{-2} at 335–345 °C. The fast neutron fluence roughly corresponds to 2 dpa with 2 He-appm in the copper specimens. With the tensile specimens, total elongations are measured and the results are shown in Fig. 4.3. The helium implanted sample shows a sharp decrease in a high-temperature plasticity of pure

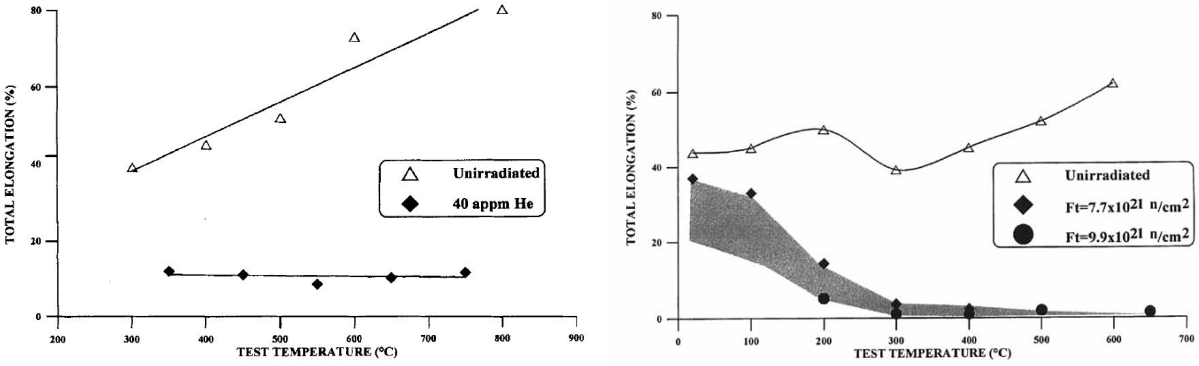

Figure 4.3: Effect of helium saturation (left) and fast neutron irradiation (right) on total elongation of pure copper [43].

copper. With dpa absent (at cyclotron irradiation) even at considerably higher helium contents of 40 appm pure copper has a 5% elongation at all temperature range tested. Under the same testing conditions pure copper irradiated in the fast neutron reactor (2 appm He) shows a 1% elongation at >340 °C. The main reason to be responsible for this brittle behavior of pure copper at >340 °C is Attributed to an effective helium accumulation at the grain boundaries during an accumulating recrystallization under irradiation.

Considering that the helium production rate in the copper thermal interface volume in the STS target is higher than the level in the test specimens presented in Ref. [43] and that the helium implant alone significantly reduced the total elonggation at all temperature range tested, we propose to assume complete loss of total elongation as design base in performing structural analyses of the target.

Chapter 5

Tungsten

5.1 SCOPE

This report summarizes material properties of pure tungsten with an aim to serve for the development and design activities to build SNS Second Target Station at ORNL.

5.2 APPLICATIONS AND TOP LEVEL REQUIREMENTS

5.2.1 APPLICATION OF TUNGSTEN IN STS

For the SNS Second Target Station, pure tungsten is selected as spallation material that produces primary neutrons by impinging high energy protons on it. Tungsten has a high neutron yield effciency thanks to its high atomic number and high mass density, and it is commercially available in large quantities.

Compared to other tungsten alloys such as densimet 18 and tungsten with 10% rhenium alloying, the pure tungsten has better residual ductilities under neutron irradiations showing the lowest degree of irradiation induced micro-structural disintegration [44]. The thermal conductivity of the pure tungsten is higher than most of tungsten and tantalum based alloys as shown in Fig. 5.1. This will result in smaller temperature gradients in the spallation volume, enabling more efficient cooling during target operation.

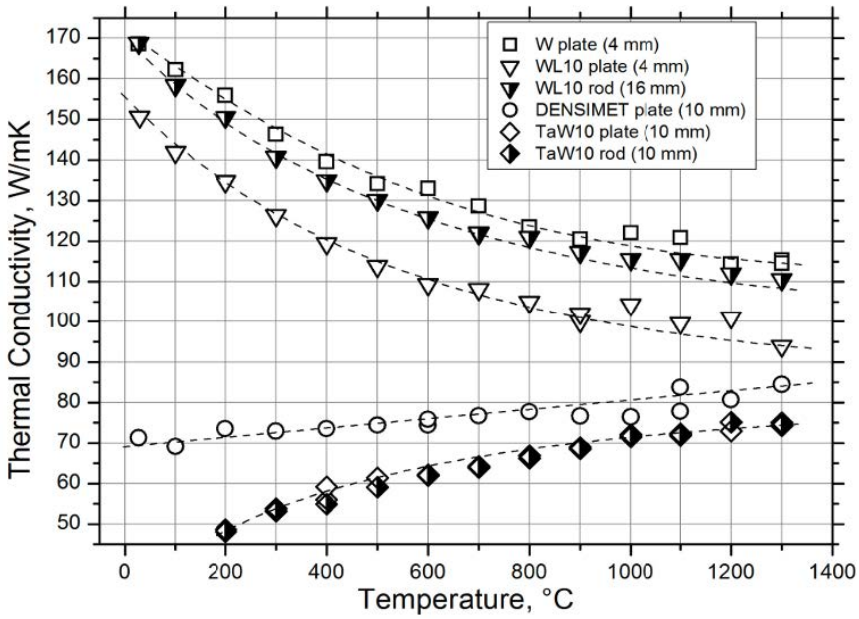

Figure 5.1: Thermal conductivity of various refractory materials [45].

5.2.2 Product Forms

5.2.3 Top Level Requirements

Density

Flexural Strength

Impurities

5.3 Lifetime Criteria

5.3.1 Fatigue Endurance Limit

5.4 Material Properties - Physical and Thermal

5.5 Material Properties - Chemical

5.5.1 Elemental Composition

The chemical composition of tungsten according to technical specification of PLANSEE SE is listed in Table 1, which is taken from Ref. [35]. The PLANSEE SE is a leading tungsten provider in the US, which can provide large volume of tungsten needed for STS target manufacturing. Therefore, elemental composition data provided in Table 5.1 will be used for shielding and activation calculations, until a final vendor is selected.

5.5.2 Oxidation

Oxidation in dry air

Oxidation kinetics of tungsten in dry air at different temperatures between 400 °C and 800 °C are studied by Druyts et al. [46] and Cifuentes et al. [47]. The oxidation kinetics is parabolic at 400 °C and 500 °C. At these temperatures, a protective oxide layer is formed on tungsten surface. The oxidation kinetics is almost linear at 600 °C, 700 °C and 800 °C. At these temperatures, volatile yellow-green oxide WO_3 is formed. However, net weight loss due to volatilization occurs at above 1000 °C in dry air. After several hours of oxidation tests in dry air at 600 °C and 700 °C [46], pure tungsten specimen foliated. This might have happened because the samples used for the test was of a hot rolled and annealed grade. Cifuentes et al. reported that cracking of the oxide scale during cooling from 700 °C to room temperature [47]. Part of the cracked scale spalled off during subsequent handling.

Oxidation in steam

In steam, tungsten initially oxidizes to tungsten dioxide by the reaction described by

$$2H_2O(g) + W(c) \rightarrow 2H_2 + WO_2(c). \tag{5.1}$$

A fraction of tungsten dioxide would be then be oxidized to form tungsten trioxide

$$WO_2(c) + H_2O(g) \rightarrow WO_3(g) + H_2, \tag{5.2}$$

which sublimates in vapor form. Tungsten trioxide is classified as inflammable solids according to GHS and it poses little concern in view of the explosion hazard risk. Tungsten dioxide could also form more volatile $WO_2(OH)_2(g)$,

$$WO_2(c) + 2H_2O(g) \rightarrow WO_2(OH)_2(g) + H_2. \tag{5.3}$$

The threshold temperature for the tungsten oxide volatilization is known to be above 700 °C and below 800 °C [48] in steam. Therefore, it is advised to keep the tungsten temperature below 700 °C during target maintenance or in loss of coolant accidents (LOCA).

Impurity Elements	Guaranteed analyses max. [μg/g]	Guaranteed analyses max. [appm]	Typical analyses max. [μg/g]	Typical analyses max. [appm]
Ag	5	8.52	5	8.52
Al	15	102.21	10	68.14
As	5	12.27	1	2.45
Ba	10	13.39	2	2.68
C	30	459.22	15	229.61
Ca	10	45.87	5	22.93
Cd	10	16.35	1	1.64
Co	10	31.20	5	15.60
Cr	10	35.35	10	35.35
Cu	10	28.93	5	14.46
Fe	30	98.77	15	49.38
H	5	910.10	1	182.02
K	10	47.02	5	23.51
Mg	5	37.81	5	37.81
Mn	5	16.73	5	16.73
Mo	100	191.62	20	38.32
N	10	131.22	5	65.61
Na	10	79.97	5	39.98
Nb	10	19.79	5	9.89
Ni	20	62.65	5	15.66
O	30	344.70	5	57.45
P	50	296.80	20	118.72
Pb	10	8.87	5	4.44
S	5	28.66	2	11.46
Si	20	130.89	10	65.45
Ta	10	10.16	5	5.08
Ti	10	38.40	2	7.68
Zn	5	14.06	5	14.06
Zr	10	20.15	2	4.03

Table 5.1: The chemical composition of pure tungsten according to technical specification of PLANSEE SE taken from Ref. [35]. The typical analyses data provided in the table will serve as the baseline chemical composition to be used for the activation calculations, until the final vendor is selected.

Hydrogen generation from steam reaction

In the presence of steam at high temperatures, tungsten reacts with steam to generate hydrogen. The reaction paths to generate hydrogen is given in Eqs. (5.1), (5.2) and (5.3). For laminar steam flow, the empirical formula for calculating the hydrogen production rate is obtained by Smolik et al. [49]. The relation for the hydrogen production rate is given as follows:

$$\dot{V}_{H_2} = 1.02 \cdot 10^5 \, P_{H_2}^{0.78} \left| \vec{v}_{H_2O(g)} \right|^{0.56} \exp\left[-1.672 \cdot 10^4 [\mathrm{K}]/T \right], \tag{5.4}$$

where the hydrogen generation rate $\dot{V}_{H_2}$ in STP-liter·m^{-2}·s^{-1}, the steam pressure P_{H_2} is in atm, the velocity of inlet steam flow $\vec{v}_{H_2O(g)}$ is in m·s^{-1} and the temperature T is in Kelvin.

For reference, the hydrogen generation rates measured for $P_{H_2} = 0.84$ atm and $\vec{v}_{H_2O(g)} = 0.037$ m·s^{-1} is plotted in Fig. 5.2, with respect to reciprocal temperature [49].

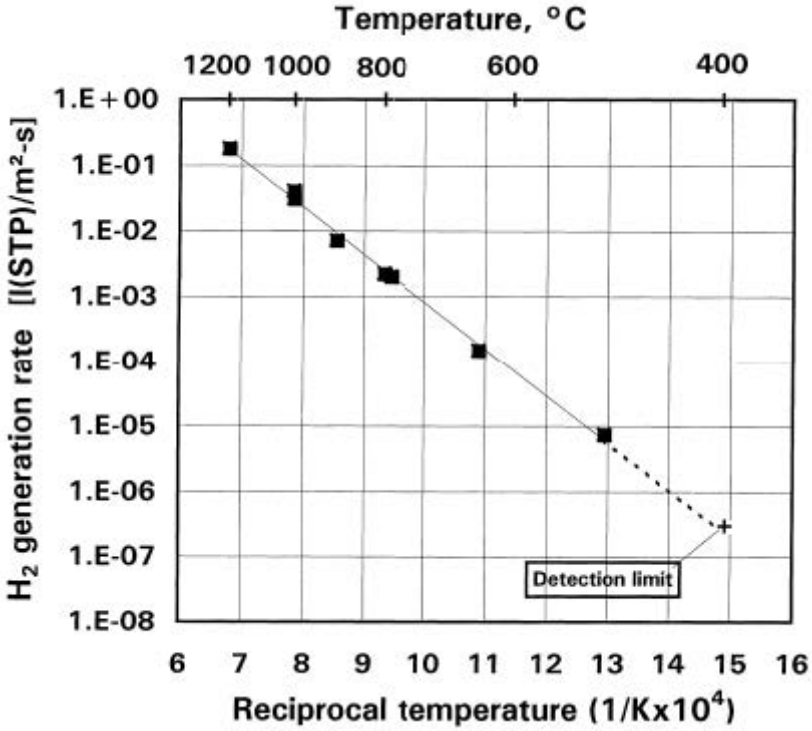

Figure 5.2: Hydrogen generation rates plotted with respect to reciprocal temperature (1/K) [49].

Pyrophoricity

Fine oxidizable tungsten powder mixed with air can constitute an explosion hazard, but the risk with tungsten powder is minimal. The self ignition temperature of tungsten powder is 310 °C [50]. Tungsten is classified as flammable solids category 1 (H228) according to GHS (Globally Harmonized System of Classification and Labelling of Chemicals [51]). Tungsten powders therefore should be kept away from heat, sparks, open flames and hot surfaces.

It has been reported in Ref. [52] that the tungsten powder with 1 µm average grain size could get ignited with a 2500 J electric discharge above minimum expressible concentration of 700 g·m^{-3}. Tungsten powder with average grain size 10 µm could not get ignited with a 2500 J electric discharge.

5.5.3 Volatilization of Tungsten at High Temperatures

Sublimation of Tungsten at High Temperatures

In the absence of oxygen or vapor, the tungsten blocks will not get oxidized. Instead, the tungsten blocks could sublimate at high temperatures. Maximum particle flux Φ_W from a tungsten block sublimation

is obtained when the ambient pressure is assumed to be absolute zero. The equation for the maximum particle flux can be derived from kinetic theory,

$$\Phi_W = 3.513 \cdot 10^{22} \frac{P_W}{\sqrt{\mathcal{M}_W T}} \quad [\text{ molecules·cm}^{-2}\text{·s}^{-1} \text{ }], \tag{5.5}$$

$$= 5.84 \cdot 10^{-2} \sqrt{\frac{\mathcal{M}_W}{T}}\, P_W \quad [\text{ g·cm}^{-2}\text{·s}^{-1} \text{ }], \tag{5.6}$$

as a function of tungsten vapor pressure P_W and the surface temperature. Here, $\mathcal{M}_W$ is molecular weight of tungsten in [g·mol^{-1}], T is surface temperature in [K] and P_W is vapor pressure of pure tungsten in [torr].

The enthalpy of tungsten evaporation and the temperature dependent tungsten vapor pressure are presented in Ref. [53] in the temperature range 2600 to 3100 K,

$$\log P_W \text{ [atmosphere]} = -\frac{45385}{T} + 7.871 \tag{5.7}$$

$$\log P_W \text{ [torr]} = -\frac{45385}{T} + 10.752 \tag{5.8}$$

$$\Delta H = 859.90 \pm 4.6 \quad \text{kJ·mol}^{-1}. \tag{5.9}$$

Table 5.2 lists the calculated values for the tungsten evaporation rates at high temperatures.

Temperature [K]	P_W **[torr]**	Φ_W **[g·cm^{-2}·s^{-1}]**
2600	$1.98 \cdot 10^{-7}$	$3.07 \cdot 10^{-9}$
2700	$8.76 \cdot 10^{-7}$	$1.34 \cdot 10^{-8}$
2800	$3.49 \cdot 10^{-6}$	$5.22 \cdot 10^{-8}$
2900	$1.26 \cdot 10^{-5}$	$1.86 \cdot 10^{-7}$
3000	$4.20 \cdot 10^{-5}$	$6.08 \cdot 10^{-7}$
3100	$1.29 \cdot 10^{-4}$	$1.84 \cdot 10^{-6}$

Table 5.2: The calculated values for the tungsten evaporation rate from a single tungsten block for chosen temperatures close to melting point.

Radio-inventory Diffusion When released from tungsten, among other isotopes produced in tungsten, the Gd-148 and the Hf-172 accounts for majority of total radiation dose to the surroundings [54]. In case of accidents, where the temperature in the tungsten blocks excurses to a high temperature, the diffusion release of these isotopes will account for the radiation dose in the monolith to a large fraction.

The diffusion constants of Gd and Hf are given by Arrhenius equation,

$$D = D_0 \exp\left(-\frac{E_A}{kT}\right), \tag{5.10}$$

where E_A is an activation energy, D_0 is a pre-exponential factor, $k = 8.61734 \cdot 10^{-5}$ eV·K^{-1} is Boltzmann constant and T is the absolute temperature. The material specific values for D_0 and E_A are compiled in Ref. [55] for selected isotopes, which include Gd and Hf. Once the diffusion constants are known, the diffusion driven release fraction f_d from a d cm thick tungsten slab can be calculated by

$$f_d \simeq 2.281 \sqrt{\frac{Dt}{d^2}}, \quad \text{for } \tfrac{Dt}{d^2} \ll 1, \tag{5.11}$$

where t is time in [s].

For reference, the calculated values for the the release fractions f_d of Gd and Hf from a 1 cm thick tungsten block is listed in Table 5.4, if the tungsten is kept at given temperature for 1 hour.

Element	D_0 [$\mathbf{cm^2 \cdot s^{-1}}$]	E_A [**eV**]
Gd	0.195	4.83
Hf	2.19	5.78

Table 5.3: The material specific values for D_0 and E_A for Gd and Hf.

Temperature [K]	f_d **for Gd at given temperature for 1 hour**	f_d **for Hf at given temperature for 1 hour**
300	1.63E-39	5.71E-47
400	2.26E-29	7.84E-35
500	2.75E-23	1.50E-27
600	3.13E-19	1.08E-22
700	2.48E-16	3.16E-19
800	3.69E-14	1.26E-16
900	1.81E-12	1.33E-14
1000	4.08E-11	5.52E-13
1100	5.21E-10	1.16E-11
1200	4.35E-09	1.48E-10
1300	2.62E-08	1.27E-09
1400	1.22E-07	8.00E-09
1500	4.65E-07	3.95E-08
1600	1.49E-06	1.60E-07
1700	4.19E-06	5.48E-07
1800	1.05E-05	1.64E-06
1900	2.37E-05	4.37E-06
2000	4.96E-05	1.06E-05
2100	9.67E-05	2.35E-05
2200	1.77E-04	4.85E-05
2300	3.09E-04	9.42E-05
2400	5.13E-04	1.73E-04
2500	8.18E-04	3.02E-04
2600	1.26E-03	5.07E-04
2700	1.88E-03	8.17E-04
2800	2.72E-03	1.27E-03
2900	3.84E-03	1.92E-03
3000	5.30E-03	2.83E-03
3100	7.16E-03	4.06E-03

Table 5.4: The calculated diffusion release fraction of Gd and Hf from tungsten blocks that are kept at given temperatures 1 hour.

Volatilization of Tungsten Oxide at High Temperatures in Moist Air

If tungsten is heated up to a temperature higher than 700 °C in moist air environment, the steam first oxidizes the tungsten surface to WO_3, hydrate it to H_2WO_4 and evaporates the tungsten hydrate [48, 56]. The empirical fit for the vaporization rate of tungsten in 100% steam is presented in Ref. [56],

$$\dot{M}_W \text{ g·cm}^{-2}\text{·s}^{-1} = A \exp\left(-\frac{\Delta H}{RT}\right) = 2611 \exp\left(-\frac{48900}{RT}\right), \tag{5.12}$$

where $\dot{M}_W$ is the rate of tungsten-metal vaporized per unit surface area, $\Delta H = 48.9$ kcal·g-mol^{-1} is the heat of vaporization, $R = 1.987$ cal·g-mol^{-1}·K^{-1} is the gas constant, and T is the tungsten surface temperature in [K]. The tungsten vaporization rate in 100% steam environment is shown in Fig. 5.3 [48].

Temperature [K]	$\dot{M}_W$ **[g·cm^{-2}·s^{-1}]**
800	1.14E-10
900	3.48E-09
1000	5.36E-08
1100	5.02E-07
1200	3.24E-06
1300	1.57E-05
1400	6.06E-05
1500	1.96E-04
1600	5.46E-04
1700	1.35E-03
1800	3.01E-03
1900	6.19E-03
2000	1.18E-02
2100	2.12E-02
2200	3.62E-02
2300	5.89E-02
2400	9.19E-02
2500	1.39E-01
2600	2.02E-01
2700	2.87E-01
2800	3.98E-01
2900	5.39E-01
3000	7.15E-01

Table 5.5: The calculated values for the tungsten evaporation rate from a single tungsten block for chosen temperatures in 100% steam atmosphere.

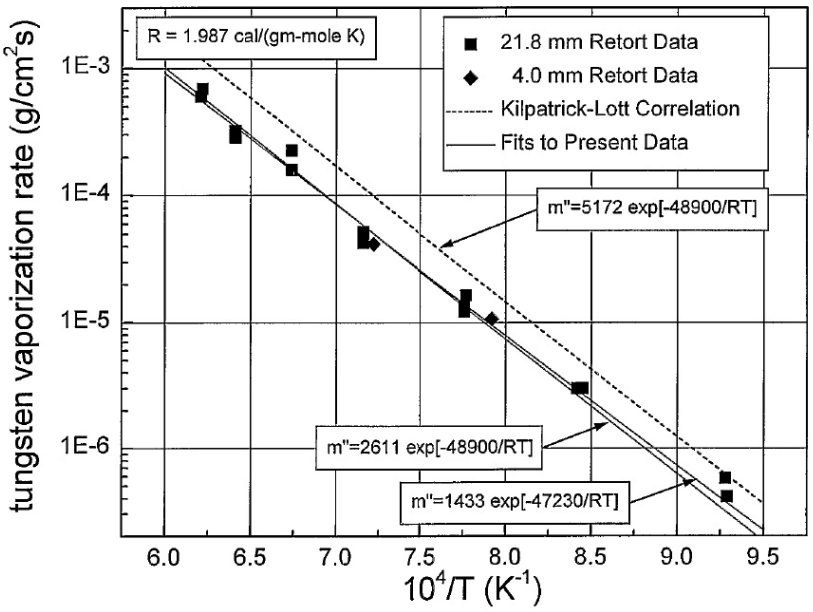

Figure 5.3: Tungsten vaporization rate in 100% steam environment [48].

Bibliography

[1] D. Aulet, Y. Dai, R. M. Bergmann, and M. Wohlmuther. Radiation damage assessment of the sixth sinq target irradiation program based on mcnpx simulation. *Nuclear Inst. and Methods in Physics Research A*, 922:310–321, 2019.

[2] Y. Dai, B. Blau, K. Geissmann, H. Schweikert, and M. Wohlmuther. The behaviour of almg3 after irradiation at high proton and neutron fluences. *Journal of Nuclear Materials*, To be published.

[3] Y. Dai and D. Hamaguchi. Mechanical properties and microstructure of $almg_3$ irradiated in sinq target-3. *Journal of Nuclear Materials*, 343:184–190, 2005.

[4] W. Lu, P. D. Ferguson, E. B. Iverson, F. X. Gallmeier, and I. Popova. Moderator poison design and burn-up calculations at the sns. *Journal of Nuclear Materials*, 377:268–274, 2008.

[5] P. L. Rittenhouse, S. A. Maloy, and M. W. Cappiello. Afci materials handbook: Materials data for particle accelerator applications. Technical Report LA-CP-06-0904 - Revision 5, Los Alamos National Laboratory, June 2006.

[6] J. R. Weeks, C. J. Czajkowski, and P. R. Tichler. Effects of high thermal and high fast fluences on the mechanical properties of type 6061 aluminum in the hfbr. In *Effects of Radiation on Materials: 14th International Symposium*, volume 2. American Society for Testing and Materials, January 1990.

[7] B. Kapusta, C. Sainte-Catherine, X. Averty, M. Scibetta, G. M. Decroix, and M. Rommens. PRESENT STATUS ON THE MECHANICAL CHARACTERIZATION OF ALUMINUM ALLOYS 5754-NET-0 AND 6061-T6 IRRADIATED AT HIGH FLUENCES. Technical Report INIS-FR-1862, CEA Saclay, May 2003.

[8] *RCC-MRx: DESIGN AND CONSTRUCTION RULES FOR MECHANICAL COMPONENTS OF NUCLEAR INSTALLATIONS*. Number ISBN 2-913638-40-6. afcen: french association for design, construction and in-service inspection rules for nuclear island components, 2012 Edition edition, 2012.

[9] Outokumpu Oyj. *Americas safety datasheet for chromium-nickel -molybdenum alloyed stainless steel*, 2 edition, November 2017.

[10] D. A. Brown and et al. ENDF/B-VIII.0: The 8^{th} Major Release of the Nuclear Reaction Data Library with CIELO-project Cross Sections, New Standards and Thermal Scattering Data. *Nuclear Data Sheets*, 148:1–142, 2018.

[11] TBM, Technical regulations for mechanical equipment. Technical Report Tech. Rep. Edition 7, Consortium of Swedish Nuclear Power Companies, 2015.

[12] D. Montierth. Email Communication on Aug. 2, 2021 with the author.

[13] J. L. Nelson. Unpublished EPRI data.

[14] A. R. Causey, G. J. C. Carpenter, and S. R. MacEwen. In-Reactor Stress Relaxation of Selected Metals and Alloys at Low Temperature. *Journal of Nuclear Materials*, 90:216–223, 1980.

[15] J. P. Foster, E. R. Gilbert, K. Bunde, and D. L. Porter. Relationship Between In-reactor Stress Relaxation and Irradiation Creep. *Journal of Nuclear Materials*, 252:89–97, 1998.

[16] O. K. Chopra and A. S. Rao. A REVIEW OF IRRADIATION EFFECTS ON LWR CORE INTERNAL MATERIALS – NEUTRON EMBRITTLEMENT, VOID SWELLING, AND IRRADIATION CREEP. Technical Report ML102010621, United States Nuclear Regulatory Commission, March 2012.

[17] R.S Lillard, D.L Pile, and D.P Butt. The corrosion of materials in water irradiated by 800 MeV protons. *Journal of Nuclear Materials*, 278(2-3):277–289, 2000.

[18] Holland Applied Technologies, https://hollandaptblog.com/2013/09/25/what-is-the-difference-between-304-316l-stainless-steel/. *What is the difference between 304 & 316L Stainless Steel?*, September 25 2013.

[19] International Atomic Energy Agency. IAEA Nuclear Energy Series Stress Corrosion Cracking in Light Water Reactors : Good Practices and Lessons Learned. Technical Report NP-T-3.13, 2011.

[20] O. K. Chopra and A. S. Rao. A review of irradiation effects on LWR core internal materials - IASCC susceptibility and crack growth rates of austenitic stainless steels. *Journal of Nuclear Materials*, 409:235–256, 2011.

[21] Bradley J. Vevera, David A. McClintock, James W. Hyres, and Bernard W. Riemer. Characterization of irradiated AISI 316L stainless steel disks removed from the Spallation Neutron Source. *Journal of Nuclear Materials*, 450:147–162, 2014.

[22] Assessment and management of aging of major nuclear power plant components important to safety: Pwr vessel internals. Technical Report IAEA-TECDOC-1557, International Atomic Energy Agency, June 2007.

[23] D. McClintock and D. Winder. Evaluation of SNS Target Post Irradiation Examination Observations and Recommendation for the Lifetime of SNS Target 27. Technical Report 106010000-TR0152 R00, Oak Ridge National Laboratory, April 2021.

[24] S. Saito, K. Kikuchi, K. Usami, A. Ishikawa, Y. Nishino, M. Kawai, and Y. Dai. Tensile properties of austenitic stainless steels irradiated at sinq target 3. *Journal of Nuclear Materials*, 343:253–261, 2005.

[25] Y. Dai, G. W. Egeland, and B. Long. Tensile properties of ec316ln irradiated in sinq to 20 dpa. *Journal of Nuclear Materials*, 377:109–114, 2008.

[26] Beryllium Products, Descriptions & Uses. Technical report, Materion Corporation: https://materion.com/products/beryllium-products.

[27] G. Muhrer, M. A. Hartl, L. L. Daemen, and J. Ryu. Benchmark test of the effectiveness of a nitrogen cooled beryllium reflector-filter. *Nuclear Instruments and Methods in Physics Research A*, (578):463–469, 2007.

[28] D. D. DiJulio, Y. Lee, and G. Muhrer. Impact of crystallite size on the performance of a beryllium reflector. *Journal of Neutron Research*, 22(2–3):275–279, 2020.

[29] ITER-EDA. Iter materials properties handbook. Technical Report ITER Document G74 MA 4 98-06-28 R 0.1, pub. pkg. #6, ITER, June 1998.

[30] ITER-EDA. Iter materials assessment report. Technical Report ITER Document GA1 DDD 1 98-05-28 W0.3, ITER, May 1998.

[31] R. Garoby and et al. The European Spallation Source Design. *Physica Scripta*, (93):014001, 2018.

[32] F. Gallmeier. Email Communication on Oct. 23, 2013 with the author.

[33] Thermophysical Properties of Materials for Nuclear Engineering: A Tutorial and Collection of Data. *Atomic Energy*, page 200, 2008.

[34] V. Chakin, J. Reimann, A. Moeslang, R. Latypov, and A. Obukhov. Thermal conductivity of highly neutron-irradiated beryllium in nuclear fusion reactors. *Progress in Nuclear Energy*, 57:2–7, 2012.

[35] ITER EDA. ITER Material Properties Handbook. Technical Report ITER Document No. S 74 MA 2, ITER, June 1998.

[36] R. E. Meredith and C. W. Tobias. *J. Electro-Chem. Soc.*, 108(3):286, 1961.

[37] S. A. Fabritsiev et al. The effect of neutron spectrum on the mechanical and physical properties of pure copper and copper alloys. *Journal of Nuclear Materials*, 233–237:526–533, 1996.

[38] T. McClanahan. Email Communication on Oct. 23, 2013 with the author.

[39] L. K. Mansur. Void swelling in metals and alloys under irradiation: An assessment of the theory. *Nuclear Technology*, 40:5–34, 1978.

[40] S. J. Zinkle. A brief review of radiation-induced cavity swelling and hardening in copper and copper alloys. In R. E. Stoller, A. S. Kumar, and D. S. Gelles, editors, *Effects of Radiation on Materials: 15th International Symposium*. ASTM International, 1992.

[41] M. Li and S. J. Zinkle. Physical and mechanical properties of copper and copper alloys. In *Comprehensive Nuclear Materials*, pages 667–690. Elsevier.

[42] S. J. Zinkle and F. A. Garner. Effect of initial oxygen content on the void swelling behavior of fast neutron irradiated copper. *Journal of Nuclear Materials*, 329–333:938–941, 2008.

[43] S. A. Fabritsiev and A. S. Pokrovsky. Neutron irradiation induced high temperature embrittlement of pure copper. *Plasma Devices and Operations*, 5:133–141, 1997.

[44] H. Ullmaier and F. Carsughi. Radiation damage problems in high power spallation neutron sources. *Nuclear Instruments and Methods in Physics Research B*, 101:406–421, 1995.

[45] M. Rieth, A. Hoffmann, E. Materna-Morris, and M. Rohde. Tungsten materials for structural divertor applications (available at http://bibliothek.fzk.de/zb/veroeff/80215.pdf). Technical report, Karlsruhe Institute of Technology.

[46] F. Druyts, J. Fays, and C. H. Wu. Interaction of plasma-facing materials with air and steam. *Fusion Engineering and Design*, 63–64:319–325, 2002.

[47] S. C. Cifuentes, M. A. Monge, and P. Pèrez. On the oxidation mechanism of pure tungsten in the temperature range 600-800 °C. *Corrosion Science*, 57:114–121, 2012.

[48] G. A. Greene and C. C. Finfrock. Vaporization of tungsten in flowing steam at high temperatures. *Experimental Thermal and Fluid Science*, 25:87–99, 2001.

[49] G. Smolik, K. McCarthy, D. Petti, and K. Coates. Hydrogen generation from steam reaction with tungsten. *Journal of Nuclear Materials*, 258–263:1979–1984, 1998.

[50] O. D. Neikov, I. B. Murashova, N. A. Yefimov, and S. Naboychenko. *Handbook of Non-Ferrous Metal Powders: Technologies and Applications*. Number ISBN: 978-1-85617-422-0. Elsevier, 2009.

[51] *Globally Harmonised System of Classification and Labelling of Chemicals*. United Nations, fourth revised edition ed. edition, 2011.

[52] K. L. Cashdollar and I. A. Zlochower. Explosion temperatures and pressures of metals and other elemental dust clouds. *Journal of Loss Prevention in the Process Industries*, 4:337–348, July 2007.

[53] E. R. Plante and A. B. Sessoms. Vapor Pressure and Heat of Sublimation of Tungsten. *JOURNAL OF RESEARCH of the National Bureau of Standards-A. Physics and Chemistry*, 77A(2):237–242, March-April 1973.

[54] Jens Harborn. Radiological Hazard Accident Scenario Analysis Target Helium cooling systems. Technical Report ESS-0039961, European Spallation Source ERIC, 2016.

[55] Eric Pitcher. Elemental Release from the ESS Tungsten Target During Normal Operation. Technical Report ESS-0044391, European Spallation Source ERIC, 2016.

[56] G. A. Greene, C. C. Finfrock, and A. L. Hanson. Behavior of High-Temperature Tungsten and Inconel in Spallation Target Applications. In *Accelerator Applications in a Nuclear Renaissance (AccApp 2003)*, June 2003.